

**Solid Sample Analysis by ICP-
Spectrometry with Femtosecond Laser
Ablation and Online Flow Digestion**

Dissertation

**zur Erlangung des Doktorgrades des
Fachbereichs Physik der Universität Dortmund**

vorgelegt von

Qunzhou Bian

Dortmund 2005

Erstgutachter: Prof. Dr. K. Niemax

Zweitgutachter: Prof. Dr. D. Suter

Tag der mündlichen Prüfung: 22. 07. 2005

Content

I. Introduction	5
II. Femtosecond laser ablation	9
1 Femtosecond laser ablation and aerosol transport	9
1.1 Interaction between laser radiation and solid states/Laser ablation	9
1.2 Material removal.....	13
1.3 Particle transport / Main mechanism of particle loss	14
2 Instrumentation and solid samples	19
2.1 Femtosecond laser system	19
2.2 Ablation stage.....	20
2.3 Inductively coupled plasma optical emission spectrometry (ICP-OES)	21
2.4 Inductively coupled plasma mass spectrometry (ICP-MS)	23
2.5 Samples used in laser ablation.....	23
3 Basic investigation of femtosecond laser ablation	25
3.1 Comparison of nano- and femtosecond laser ablation	25
3.2 Analysis of femtosecond laser-irradiated region	27
4 Femtosecond LA-ICP-OES	29
4.1 Experimental.....	30
4.2 Comparison of transient Zn and Cu signals.....	31
4.3 The dependence of the Zn/Cu ratio on time and fluence	34

4.4 Non-matrix matched calibration	36
4.5 Summary.....	38
5 Femtosecond LA-ICP-MS	39
5.1 Experimental	40
5.2 Investigation of ion spatial distributions in an ICP	40
5.3 Matrix effect on the Zn/Cu ratio	44
5.4 Laser fluence effects on the Zn/Cu ratio	46
5.5 Summary	48
III. Flow digestion of solid sample.....	49
6 Introduction of solid sample digestion	49
7 Instrumentation.....	55
7.1 Flow digestion system and gas removal interface	55
7.2 ICP-OES and HG/CV-AAS	57
8 Investigation of the digestion system.....	59
8.1 Digestion conditions	59
8.2 Lifetime of the Pt/Ir Capillary.....	61
8.3 Element recovery	62
8.4 Gas effect.....	64
8.4.1 The influence of reaction gas on the pressure in the system	64
8.4.2 The influence of reaction gas on ICP-OES analysis	66
8.4.3 The influence of reaction gas on HG/CV-AAS analysis	67
9 Investigations of gas removal	69
9.1 Optimization of the gas removal interface.....	69
9.1.1 Silicon/Ceramic tube	71
9.1.2 Polypropylene tube.....	71
9.2 Gas removal efficienc	73
10 Online coupling of the flow digestion system with ICP-OES	77
10.1 Experimental	77
10.2 Connection between polypropylene tube and a nebulizer	78
10.3 Signal collecting mode	79
10.4 Sample determination.....	80

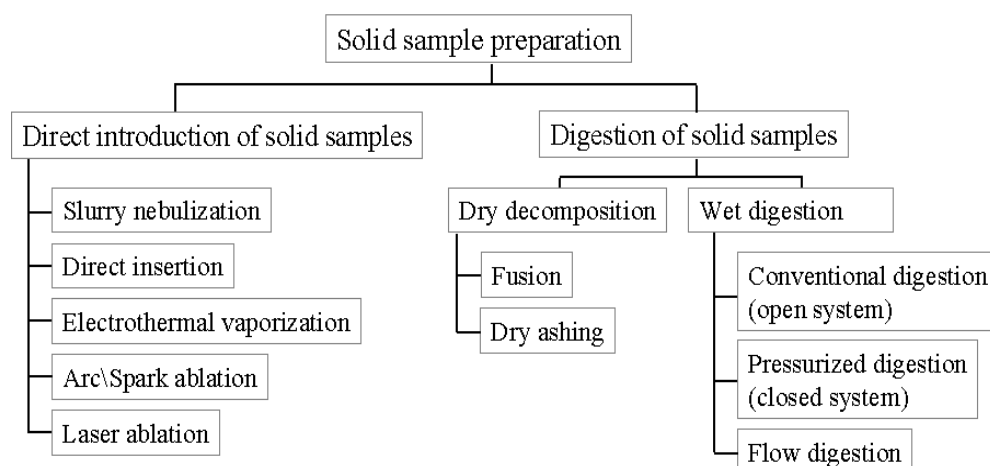
10.5 Sampling frequency.....	83
11 Online coupling of the flow digestion system with HG/CV-AAS	85
11.1 Optimization of operation conditions.....	85
11.1.1 Optimization of carrier gas flow rate	86
11.1.2 Optimization of the NaBH ₄ concentration	87
11.1.3 The effect of cooling the inlet arm of T-shaped quartz tube	88
11.2 Arsenic analysis	89
11.3 Mercury analysis	90
IV. Conclusion.....	93
Bibliography	97
Acknowledgements.....	101

I. Introduction

Atomic emission and atomic mass spectrometry are powerful tools for rapid element analysis. Nowadays in particular the inductively coupled plasma (ICP)-based spectrometry, e.g. inductively coupled plasma mass spectrometry (ICP-MS) and inductively coupled plasma optical emission spectrometry (ICP-OES), have become routine analytical methods for many applications, such as analyses of biological and environmental samples, elemental determinations in metals and alloys, and analyses of glasses and other hard materials [1- 3]. The tremendous success of these techniques is based on the distinguished capability of the ICP as the excitation and ionization source. When aerosol or gas samples pass through the plasma, a series of processes such as vaporization, atomization and ionization occur in sequence to generate large quantities of atoms and ions for analyses. Usually, gases and liquid samples are easy to be introduced to the ICP. However, for solid samples, this is not always true, which limits the applicability of ICP-MS and ICP-OES for elemental analysis of solid materials [4, 5].

As shown in the following figure, a solid sample is either digested to form a solution for introduction applying a nebulization method or introduced directly using some specific techniques. Traditional dissolving methods need multi-step, labour-intensive and time-consuming procedures, no matter whether they work under atmospheric pressure or high pressure [6- 9]. Therefore, it is necessary to develop faster and more efficient online solid sample digestion systems to eliminate the complicate and time-consuming preparation procedures that also can cause analytical errors. Alternatively, some direct introduction techniques, such as electro-thermal vaporization (ETV) [10, 11], arc ablation

[12] and spark ablation [13], have been developed for direct solid analyses, but these methods still have some intrinsic drawbacks. Direct solid sampling using nanosecond pulsed laser ablation (ns-LA) has been demonstrated to be a promising way for fast solid analysis with ICP-based spectrometers [14-16]. Recently, femtosecond (fs) lasers have been applied for the first time in analysis [17-19]. Femtosecond lasers show great advantages over nanosecond lasers because the ultra-fast interaction with solid targets generates very fine aerosols [20, 21], whose composition is identical with the bulk composition and which can be transported without significant losses over large distances. This is different from ns-LA where a significant fraction of particles are large and may be lost during the transport to the ICP. Therefore, fs LA seems to be a better choice for LA-ICP- spectrometry.



Preparation and introduction approaches for solid samples

The objective of this thesis is the improvement of the accuracy in ICP-spectrometry applying two sample preparation techniques: direct solid sampling using laser ablation and flow digestion under high-temperature/high-pressure conditions. In the first case, a near-infrared (NIR) femtosecond laser system with 100 fs pulse-width is used to ablate material in a noble gas filled cell. The generated aerosols are transported by a gas stream to the ICP spectrometer to study the potential capability of the ultrashort-pulsed laser as an ablation source in non-matrix matched solid sample analyses. The spatial distributions of ions within the plasma have also been studied by ICP-MS. In the second case, a high-temperature/high-pressure digestion system is designed for flow digestion of biological

and environmental samples, and an interface for effective coupling of the digestion system with the ICP is developed for online elemental determination.

In order to compare different ablation effects using femtosecond laser and nanosecond laser, the aerosols ablated from brass alloys using both lasers at different laser fluences are analyzed using an ICP-OES spectrometer. The crater profiles and ablation efficiency are also investigated for dielectric and metallic samples.

Although solid sampling with laser ablation exhibits great advantages for ICP-MS and ICP-OES analyses, the lack of suitable solid standards still limits their application in accurate analyses of solid samples [22]. Non-matrix matched analyses would be a major breakthrough in the use of laser ablation. Femtosecond pulsed lasers tend to produce stoichiometric aerosols in ablation of solid materials, i.e. aerosols which in total have the same element composition as the bulk [23]. The prospects of femtosecond laser ablation for the non-matrix matched analyses of solid samples will be evaluated in this work. Matrix effects on both signal structure and elemental fractionation are studied by analyzing Zn and Cu elements using ICP-OES, whereas brass alloys, Al alloys and silicate glasses were chosen to prove the matrix independence of the method.

In elemental analyses using ICP-MS instruments, only a very small fraction, usually $1/10^6$ to $1/10^8$ of the ions produced in the plasma can reach the detector. The analysis using LA-ICP-MS spectrometry risks an unrepresentative ion extraction from the ICP ion reservoir because of different ionization behaviours of different sized aerosols and different thermal volatilities of different elements. The spatial distributions of ions within the ICP will be studied in femtosecond laser ablation of metallic materials. Matrix effects on Zn/Cu ratio at different positions of the ICP will be investigated and laser fluence effects will also be compared in analysis of metallic and dielectric samples.

A temperature of 300 °C is necessary for complete digestion of organic compounds in most biological and environmental materials [24]. In order to realize the rapid sample digestion, a compact high-temperature/high-pressure (HTHP) flow digestion system with electrically heated Pt/Ir or Ta capillary has been designed and tested in detail. The influences of the gaseous reaction products (CO_2 , NO and NO_2), formed by the oxidation of biological and environmental samples in nitric acid during the sample digestion process, on the digestion system and elemental determinations will be discussed.

A direct coupling of the sample digestion system with the ICP-based spectrometer was unsuccessful because of severe interference of the gaseous reaction products to the plasma. Different types of gas-permeable tubes have been used to degas the sample solution in the reported experiments. A new interface with a minimum dead volume, high efficient gas removal and high sample throughput has been developed and optimized. Finally, elements in various biological and environmental materials are determined online to evaluate the accuracy and reliability of the coupling of the digestion system with the detection instruments via this interface.

II. Femtosecond laser ablation

Chapter 1

Femtosecond laser ablation and aerosol transport

This chapter provides basic information concerning the sampling process applying femtosecond laser pulses as well as the transport of aerosol particles formed during ablation. It consists of three parts: a theoretical description of the interaction between laser radiation and solid samples, the depiction of particle ejection, and an introduction to the transport properties of laser-produced aerosols involving the discussion of different processes responsible for material loss.

1.1 Interaction between laser radiation and solid states/Laser ablation

Laser ablation of solid states generally implies the conversion of optical into thermal energy via electronic excitation, followed by the vaporization and ejection of species from the irradiated volume [25].

In fact, laser radiation can effectively interact only with electrons located in the conduction band of a solid state. Therefore, the mechanisms of energy absorption are supposed to vary strongly for dielectric and metallic materials. Regarding metals (or semiconductors) the laser energy can directly be absorbed by the process of inverse Bremsstrahlung because of their large initial number of free electrons ($n \sim 10^{23} \text{ cm}^{-3}$) [26]. The absorption coefficient can be described by [27]

$$\alpha_{IB} \approx C \cdot \lambda^3 \frac{Z^2 N_i N_e}{T_p^{1/2}} \left[1 - \exp\left(-\frac{\hbar\omega}{k_B T_p}\right) \right], \quad 1.1$$

where $C \approx 1.37 \times 10^{-35}$, \hbar is Planck constant, k_B Boltzmann constant, λ the wavelength in μm , Z the average ion charge, N_i and N_e the number densities of ions and electrons, T_p the plasma temperature and ω the frequency.

However, energy deposition in wide-band-gap materials requires the build-up of a certain density of “seed” electrons inside the conduction band since its thermal population is usually too small (especially in the absence of intrinsic defect states). If the photon energy is less than the band gap, electronic inter-band transitions must be induced via a non-resonant multi-photon absorption (MPA) and avalanche ionization (AI) [28-30]. The number of photons required for MPA is determined by the smallest amount m that satisfies the relation

$$m\hbar\omega > E_g, \quad 1.2$$

where E_g is the material-specific band-gap and $\hbar\omega$ the energy of the laser photons. After the creation of those “seed” electrons, rapid heating occurs [31] and once the thermal energy kT reaches E_g , secondary electron excitation by AI superimposes MPA. Under the combined action of MPA and AI, large quantities of electrons are then transferred to the conduction band ^[i].

If a sufficient number of free electrons are present, the incoming pulse energy can efficiently be absorbed by inverse Bremsstrahlung to transient temperatures of around 10^4 K (as in the case of metals or semiconductors). Corresponding heating rates are approximately 10^{14} K/s. Thus, electron heating is accomplished within a few hundreds of

ⁱ For longer laser pulses, “seed” electrons can also be generated by thermal excitation from traps or defect states formed during laser-matter-interaction.

femtoseconds, as indicated in Fig. 1.1. However, the subsequent energy transfer to the lattice is more time-consuming. According to ref. [29, 32] lattice heating, which is controlled by the strength of the electron-phonon coupling, happens on a timescale ranging from a few up to several tens of picoseconds, depending on the material considered.

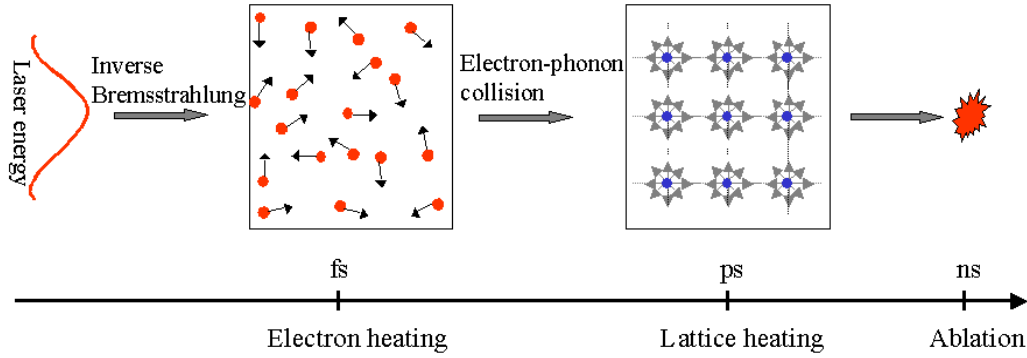


Figure 1.1 Energy transfer process from optical to thermal energy on a timescale ranging from femtosecond (energy absorption) to nanosecond duration (onset of ablation). (from ref. 29, 32)

In case of nanosecond laser ablation, the pulse duration is by far larger than the lattice heating time. Therefore, the laser-solid interaction is of adequate time to deposit energy not only in the irradiated zone, but also in its neighboring volume due to strong thermal diffusion. The corresponding heat penetration depth is given by $l \sim (\tau D)^{1/2}$, which depends on the heat diffusion coefficient D of the material and the pulse duration τ [26].

For pico- or femtosecond laser pulses, τ usually falls below the electron cooling time. Phonon excitation due to electron-phonon coupling and subsequent solid-liquid phase transitions is therefore confined to the irradiated zone. The perimeter of zone heating in this limiting case is determined by electron diffusion that is on the order of 100 nm. Heat transfer as a result of phonon migration out of volume can completely be neglected. Nevertheless, inside the irradiated volume, electron-phonon coupling eventually results in the decomposition of the lattice structure as the material-specific critical point has been reached and material ejection takes place (see below) ^[iii].

Quantitatively, the interaction of ultra-short laser pulses with solid states can be described by the two-temperature model [33-35] which treats the heat conduction for

ⁱⁱ The energy loss that is induced by zone heating also affects the ablation threshold in case of nanosecond pulses because the intensity is too small to compensate for energy loss caused by thermal diffusion out of the volume.

electrons and lattice separately. First, the laser energy is absorbed by free electrons, which brings an immediate temperature rise, while the lattice still remains at ambient temperature. Then, the energy is delivered to the lattice because of the temperature gradient. After that, both electron and lattice temperatures equilibrate. A schematic diagram is given in Fig. 1.2 showing the processes of laser-matter interaction for femtosecond ablation.

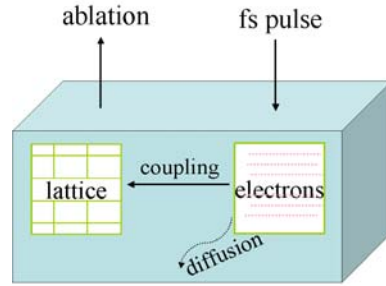


Figure 1.2 Schematic diagram of the laser-matter interaction using femtosecond pulses.

(From ref. [26])

According to the two-temperature model, the electron temperature (T_e) and the lattice temperature (T_i) can be described by the following equation system 1.3:

$$\begin{aligned}
 C_e \frac{\partial T_e}{\partial t} &= -\frac{\partial Q(z)}{\partial z} - \gamma(T_e - T_i) + S, \\
 C_i \frac{\partial T_i}{\partial t} &= \gamma(T_e - T_i), \\
 Q(z) &= -k_e \partial T_e / \partial z, \quad S = I(t) A \alpha \exp(-\alpha z),
 \end{aligned}
 \tag{1.3}$$

where z is the direction perpendicular to the target surface, $Q(z)$ the heat flux, S the laser heating-source term, $I(t)$ the laser intensity, A and α are surface absorptivity and the material absorption coefficient, respectively; C_e and C_i are the heat capacities (per unit volume) of the electron and lattice subsystems, γ is the parameter characterizing the electron-lattice coupling, and k_e the electron thermal conductivity.

During the process of femtosecond laser heating, the electron-lattice coupling can be ignored. At the end of a laser pulse, the electron temperature can be calculated when ignoring the electron heat conduction term. Then, the electrons are rapidly cooled during the energy transfer to the lattice, resulting in an attainable lattice temperature (T_i) described by [34]

$$T_i \cong \frac{F_a}{C_i} \frac{l}{l^2 - \delta^2} [l \exp(-z/l) - \delta \exp(-z/\delta)], \quad 1.4$$

where $l = (\tau D)^{1/2}$ is the electron heat penetration depth, $\delta = l/\alpha$ the skin depth and $F_a = E(I - R)/A$ the absorbed fluence. The equation can be approximated into two limiting cases: the low and high fluence regime. At low fluences, the energy can only be transferred to the lattice within the skin depth, while at high fluences, electron heat penetration depth becomes dominant. The corresponding temperature distributions are given by [34]

$$T_i \cong \frac{F_a}{C_i \delta} \exp(-z/\delta) \quad (\delta \gg l), \quad 1.5$$

$$T_i \cong \frac{F_a}{C_i l} \exp(-z/l) \quad (\delta \ll l). \quad 1.6$$

A significant evaporation can occur if $C_i T_i$ becomes larger than $\rho \Omega$, where ρ is the density and Ω the specific heat of evaporation (per unit mass). The ablation depths (L) per pulse is given by

$$L \cong \delta \ln(F_a / F_{th}^\delta), \quad F_{th}^\delta \cong \rho \Omega \delta \quad (\delta \gg l), \quad 1.7$$

$$L \cong l \ln(F_a / F_{th}^l), \quad F_{th}^l \cong \rho \Omega l \quad (\delta \ll l), \quad 1.8$$

with the ablation thresholds F_{th}^l and F_{th}^δ for the low and high fluences, respectively. The ablation rates (expressed as the ablation depth L per laser pulse) follow approximately a logarithmic fluence dependence.

1.2 Material removal

Compared to the excitation processes described above, material removal, i.e. ablation from the surface of the target lasts up to the nanosecond regime [29]. According to the two-temperature model, the lattice can be heated up to temperatures close to or well above the critical temperature within several picoseconds, even for moderate laser intensities. This results in the formation of a hot and pressurized fluid state. Explosive

boiling and critical-point phase separation (CPPS) are considered to be the primary mechanisms of material removal during laser ablation [25].

Explosive boiling takes place at a temperature close to the critical temperature of the material [25, 36]. Lots of bubbles are spontaneously formed via homogeneous nucleation in the superheated region. Subsequently, a rapid transition from the overheated liquid into a mixture of vapor and liquid droplets is undergone. This process is assumed to apply for both nano- and femtosecond laser ablation.

In contrast, critical-point phase separation (CPPS) is discussed in conjunction with material removal by ultra-short pulses only [25]. Clear separation occurs via a so-called spinodal decomposition involving thermodynamic instabilities close to the critical point [37]. Material from the uppermost layer can be directly transferred to vapor phase due to its high temperature, whereas small amounts of droplets are ejected at the end of this process.

1.3 Particle transport / Main mechanism of particle loss

For analysis using ICP-MS/OES, laser-produced aerosols need to be transported out of the ablation chamber by a carrier gas flow. During the transport, particle loss mainly occurs as a result of diffusion, gravitational settling, inertial deposition, and electrostatic deposition.

Aerosol diffusion is caused by collisions with the carrier gas molecules in which the particle is suspended. The diffusion is supposed to be negligible for bigger particles because of counteracting collisions from different directions. However, small particles might obtain a net-momentum because they collide only with a comparatively small number of gas molecules. Diffusion is generally described by Fick's first law [38]

$$J = -D \frac{\partial C}{\partial x} \quad , \quad 1.9$$

where J is the rate of diffusion, $\partial C/\partial x$ the particle concentration gradient, and D the diffusion coefficient, which is given by the Stokes-Einstein equation [38, 39]

$$D = \frac{KTC_c}{3\pi\mu d_p}, \quad 1.10$$

where k is the Boltzmann constant, T the temperature, C_c the Cunningham slip correction factor (which is a function of particle diameter and the gas mean free path), μ the gas viscosity, and d_p the particle diameter.

Regarding aerosol transportation through a cylindrical tube under laminar flow conditions, diffusion losses η_d can be approximated by [23, 40]

$$\eta_d = 1 - 0.8191 e^{-3.657\xi} - 0.0975 e^{-22.3\xi} - 0.0325 e^{-57\xi} + \dots \quad 1.11$$

for $\xi > 0.0156$, and

$$\eta_d = 2.56 \xi^{2/3} - 1.2\xi - 1.77 \xi^{3/4} \quad 1.12$$

for $\xi < 0.0156$, in which ξ is given by

$$\xi = \frac{lk_B T}{3\mu d_p V}, \quad 1.13$$

here, l denotes the length of the tube, T the gas temperature, V the flow rate through the tube, μ the viscosity, and d_p the particle diameter. Apparently, diffusion results in the selective loss of smaller particles.

In contrast to diffusion, gravitational settling applies to particles larger than about 1 μm . According to ref [41] losses caused by gravitational settling are given by

$$\eta_{gs} = 1 - \exp\left(-\frac{4gC_c\rho r^2 L \cos\phi}{9\pi\mu Rv}\right), \quad 1.14$$

where g is the gravitational constant, ρ the density of the particle, r its radius, ϕ the inclination angle relative to horizontal, R the tube radius, μ the viscosity of the fluid, and v the carrier gas flow rate. At atmospheric pressure, for instance, 1 and 10 μm particles settle at about 30 μm and 3 mm per second, respectively.

Electrostatic settling only occurs if transported particles are pre-charged and an electrostatic field has been built up across the transportation tube or interfacing parts of the transport system. In order to assess the potential risk of material loss due to electrostatic settling during transportation the aerosol charging of different particle sizes,

ranging from 10 nm up to 4 μm , has recently been studied for laser ablation of Si (Fig. 1.3) [42]. The induced current signals were measured by electrostatic low-pressure impaction using a commercial 12-stage cascade impactor. Corresponding charging plots are calculated from the currents measured and mass distribution quantified by total reflection X-ray fluorescence (TXRF). It has been shown that the number of elementary charges critically depends on the particles size and that larger particles carry by far more charges. Unlike most of the other mechanisms of particle loss, electrostatic effects can easily be circumvented using conducting surfaces that are properly taken to the ground.

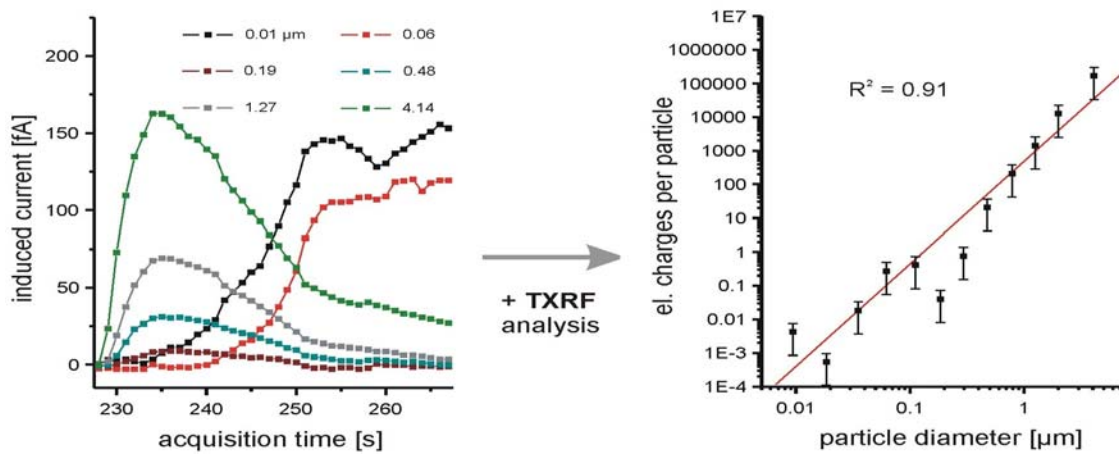


Figure 1.3 Transient current signals (6 channels) as well as the corresponding charging plot of laser-produced Si particles (from ref. 42). (For small particles only statistical charging happens i.e. every tenth or hundredth particle carries one elementary charge)

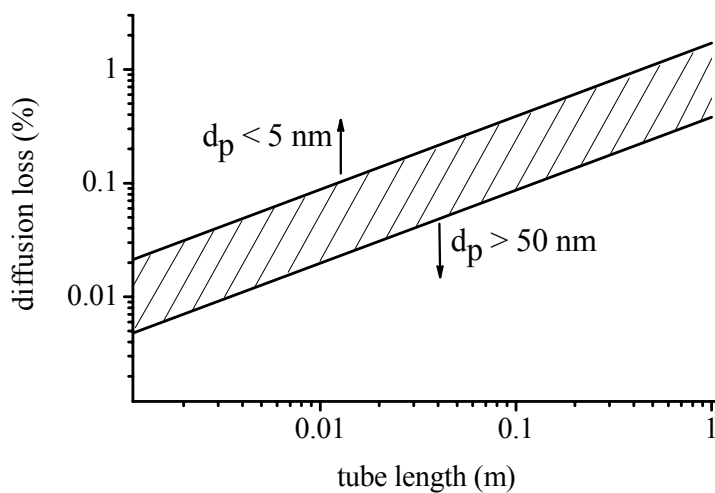


Figure 1.4 Diffusion losses of particles with a diameter between 5 and 50 nm as a function of the transport distance assuming a flow rate of 1 L/min. (from ref. [23])

The above-mentioned mechanisms of material loss are size-dependent. Gravitational settling and inertial deposition are valid for larger particles, while diffusion is dominant for small particles. As shown in ref. [43] femtosecond laser ablation of solids enables to produce mesoscopic-sized particles which are (i) on the one hand too big to undergo substantial diffusion losses and are (ii) on the other hand too small to be subject to inertial or gravitational settling. Nevertheless, macroscopic aerosol charging may result in the occurrence of repulsive forces inside the propagating aerosol cloud implying that electrostatically enhanced diffusion might be the dominant origin of particle loss during transportation though the over-all losses are negligible. In Fig. 1.4 the calculated diffusion losses (according to equation 1.11 and 1.12) of a typical, non-charged aerosol consisting of particles with a diameter between 5 and 50 nm applying a flow rate of 1 L/min is shown. As can be seen, the loss is smaller than 2% even for transport distance of 1 m [23].

Chapter 2

Instrumentation and solid samples

This chapter presents the main instruments and the solid samples which were used in this section. The experimental setup consists of a femtosecond laser, an ablation stage, and ICP-based spectrometers.

2.1 Femtosecond laser system

A CPA-type femtosecond laser system operated at a wavelength of 795 nm (Hurricane, Spectra Physics, Mountain View, USA) has been employed for ablation of solids. It is a regenerative amplifier system including a Mai Tai seed laser (a diode-pumped cw laser and a mode-locked Ti: Sapphire pulsed laser), an Evolution pump laser (a diode-pumped Q-switched Nd: YLF laser) and the “Spitfire” (a stretcher, a compressor and a regenerative amplifier (RA)). Fig. 2.1 shows its structure and the formation process of a femtosecond pulse.

A diode-pumped cw laser pumps a cw mode-locked Ti: Sapphire oscillator, which produces a few nanojoules (approximately 800 mW) of ultra-short pulses. These pulses are transferred to the Spitfire to be stretched, amplified and then recompressed, resulting in over 1 mJ of ultra-short pulses, which represents an overall amplification of greater than 10^6 . The technical characteristics of the femtosecond laser system are summarized in Table 2.1.

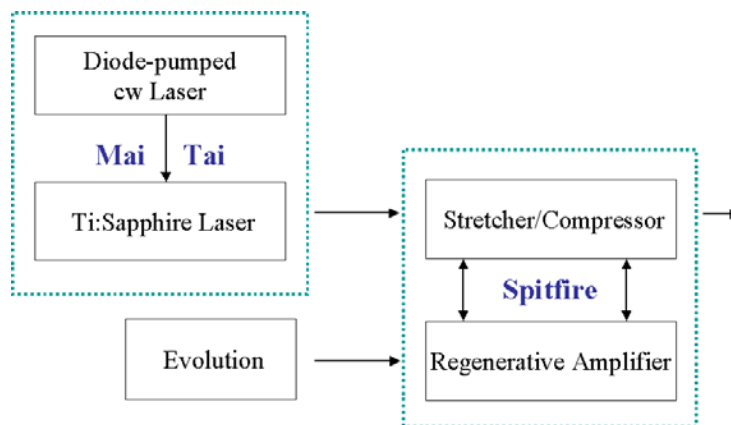


Figure 2.1 Schematic diagram of Hurricane-Ti: Sapphire amplification system.

Table 2.1 Technical characteristics of the Hurricane femtosecond laser

Repetition rate	1 kHz (maximum)
Pulse duration	About 100 fs
Energy @ 1 kHz	>750 μ J
Wavelength	795 nm
Beam diameter	5 mm
Beam profile	Gaussian
Contrast ratio	Pre-pulse > 1000:1 Post-pulse > 100:1
Spatial mode	< 1.5 x diffraction limited
Energy stability ($\pm\%$ p/p)	< 3%

2.2 Ablation stage

A laser ablation unit, schematically shown in Fig. 2.2, comprises a lens and an ablation chamber. Samples to be analyzed are fixed by a holder, which is placed in the center of the cylindrical ablation cell ($V = 20 \text{ cm}^3$). The sample position is adjusted using a two-dimension translation stage with manual controls integrated in the bottom of the cell. The laser beam is delivered through a plano-convex lens ($f = 100 \text{ mm}$) by high reflecting mirrors and subsequently focused onto the sample surface, the focus position can be changed by shifting the lens along the beam axis. The cell outlet was connected to the ICP torch via a PTFE tube (length: 35 cm, i.d.: 4 mm). Helium is applied to flush the aerosol particles out of the cell as it has been found to provide optimum performance concerning aerosol size distribution and suppression of laser-induced fractionation [23].

An additional amount of Ar was admixed via a Y-type interface right behind the cell outlet.

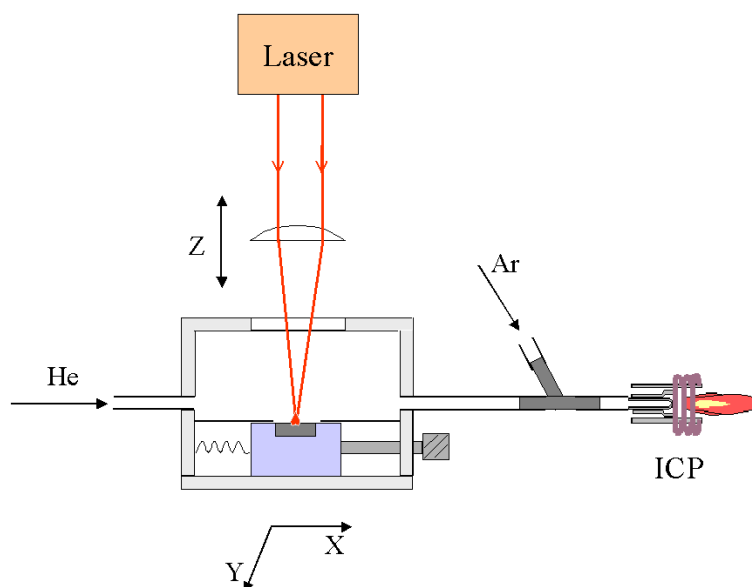


Figure 2.2 Arrangement of the laser ablation unit.

2.3 Inductively coupled plasma optical emission spectrometry (ICP-OES)

ICP-OES is a well-known technique with high potential for elemental analyses. Its principle is based on the detection of line spectra emitted by excited atoms or ions. The major advantage is its simultaneous multi-element detection ability. The detection limits typically lie in the range of ppm to ppb.

Femtosecond LA-ICP-OES is performed with a commercial ICP-OES instrument with axial observation of the plasma (IRIS/AP, Thermo Jarrell Ash, Franklin, MA, USA). The instrument schematically shown in Fig. 2.3 is equipped with two multichannel detectors of charge injected device type (CID), one is a low-wavelength detector ($\lambda < 360$ nm) while the other detects the lines with longer wavelengths ($\lambda \geq 360$ nm).

The signals are collected in a time-resolved mode by the CID detectors (time study). 1 s integration time and 10% signal increment are used for all experiments to control the actual signal integration time and to avoid detector saturation. The highest possible RF-

power of the instrument (1350 W) is applied to generate a sufficient gas temperature in the central channel of the plasma.

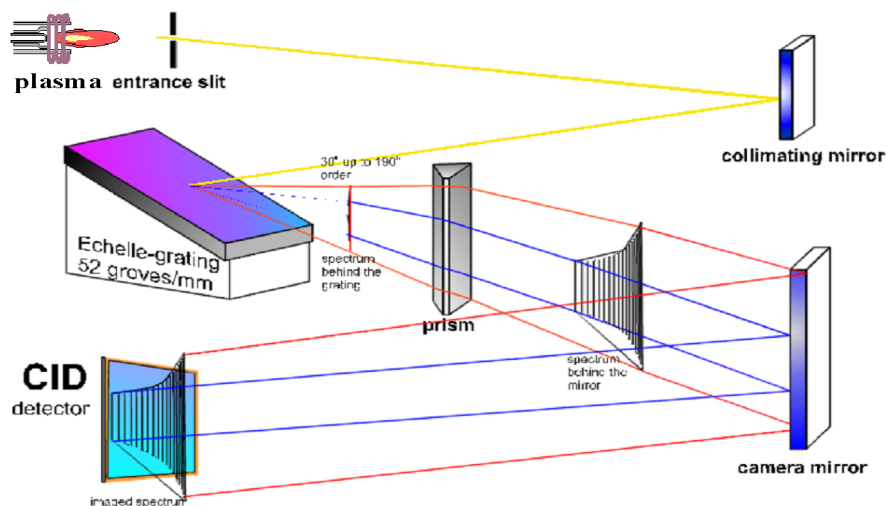


Figure 2.3 Schematic diagram of the ICP-OES with axial observation of the plasma. (From Thermo Jarrell Ash Corporation)

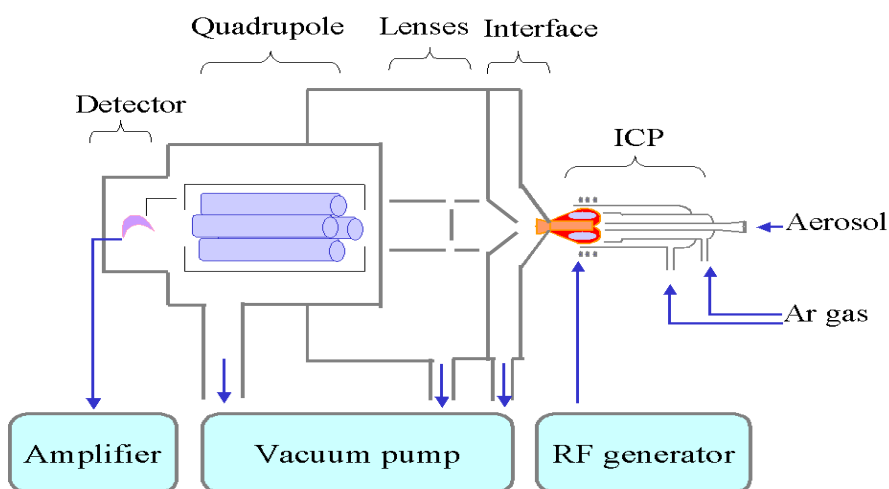


Figure 2.4 Schematic diagram of the ICP-MS.

2.4 Inductively coupled plasma mass spectrometry (ICP-MS)

Laser ablation (LA) coupled with ICP-MS has become a popular method for the detection of elements in solid samples due to its low detection limits [44.- 47]. ICP-MS is a fast sequential detection technology, which is based on the generation of atomic ions within the plasma. Ion sampling of the plasma is accomplished using an interface including a sampler cone and a skimmer cone. A series of cylindrical electrodes behind the cones are designed to extract and focus ions. Finally, ions of selected mass-to-charge ratios (m/z) are transmitted to a detection system by the quadrupole mass filter.

The PQ2 ICP-MS (VG ELEMENTAL) has been used in the experiments. A schematic diagram showing the main functional components within the instrument is given in Fig. 2.4. The instrument consists of five key parts, namely the ICP ion source, the interface between the plasma and the mass spectrometer (sampler cone and skimmer cone), ion transfer optics, the quadrupole mass filter (QMF) and the ion detector with a channel electron multiplier. Ion detection is achieved by a pulse-counting technique or by an analog measurement.

2.5 Samples used in laser ablation

Among the samples under investigation, brass certainly represents the most critical material with respect to the different thermal volatilities of its main constituents Zn and Cu. In contrast, Al is distinguished by a relatively low melting but high boiling point. Silicate glass was chosen as a typical representative of dielectric materials since it combines amorphous structure, non-conductivity, as well as thermal and chemical resistivity. Apparently, these matrices cover a wide spectrum of physical properties and are therefore good candidates for solid analysis using LA-ICP spectrometry.

The compositions of brass, Al and silicate glass samples are shown in Table 2.2. Before analysis, the sample surfaces were polished down to 1 μm roughness using sandpaper and diamond suspensions of different grain size.

Table 2.2 Zn and Cu compositions of the brass, Al alloy, and silicate glass standards

Matrix	Zn [%]	Cu [%]	Zn/Cu
Brassⁱ			
NBS 1113	4.8	95.0	0.050
TD-02	19.7	80.3	0.25
TD-03	29.8	70.2	0.42
TD-04	34.5	65.5	0.53
TD-06	39.4	60.6	0.65
TD-07	41.9	58.1	0.72
Al alloyⁱⁱ			
AZ-3	6.05	1.75	3.46
VAW-3414	9.20	1.20	7.67
Silicate glassⁱⁱ			
Glass no. 1	-	-	10.82 ⁱⁱⁱ
Glass no. 2	-	-	9.61 ⁱⁱⁱ
Glass no. 3	-	-	7.70 ⁱⁱⁱ
NIST 610	433 (mg/kg)	444 (mg/kg)	0.97

ⁱ Wieland Werke AG, Ulm, Germany

ⁱⁱ Breitländer GmbH, Hamm, Germany

ⁱⁱⁱ Ratio determined by TXRF analysis / According to the manufacturer the absolute Zn and Cu contents are in the range of a few percent

Chapter 3

Basic investigation of femtosecond laser ablation

3.1 Comparison of nano- and femtosecond laser ablation

Most applications of laser ablation have been done with nanosecond lasers. However, nanosecond lasers have been found to form the so-called “heat-affect zones” which are caused by thermal diffusion into the target. Consequently, elemental fractionation due to fractional evaporation and material re-distribution can occur even if the local temperature is high enough to evaporate the most refractory elements. Moreover, a part of the pulse energy is dissipated above the exposed area that, in turn, may affect the composition of aerosol particles formed during material expansion. Zone heating and plasma shielding are obviously both related to the pulse duration, which governs the ablation process [48]. In contrast, femtosecond lasers show great advantages over nanosecond lasers in interaction with solid materials. Furthermore, stoichiometric aerosols (aerosols which have the same composition as the bulk) are ablated [23, 48]. This significantly improves the analysis performance of an ICP-based spectrometer.

The femtosecond laser, described in Chapter 2, and a nanosecond laser (surelite Nd/YAG laser from Fa. Continuum) with pulse duration of 10 ns have been used to generate aerosols for analyses using an ICP-OES spectrometer. Similar operating

conditions related to the laser ablation, aerosol transport and the ICP-OES instrument were applied for both cases.

The transient signals of Zn 202 nm and Cu 224 nm were recorded during ablation of the brass TD-07 using nano- and femtosecond lasers. The corresponding Zn/Cu intensity ratios are shown in Fig. 3.1. The ratios shown in Fig. 3.1 (a) were obtained by ns LA at fluences from 5 to 20 J/cm². They were different but constant during the analysis time of 50 s or even more. The Zn/Cu ratio decreased with increasing fluence. There is a significant enhancement of volatile Zn in ns LA of a brass alloy, which can be reduced with high fluence. In contrast, when the femtosecond laser was applied to brass TD-07 at fluences up to 8.2 J/cm², the Zn/Cu ratios were independent of the laser fluence (see Fig. 3.1 (b)). Furthermore, the Zn/Cu ratios were much lower than at nanosecond laser ablation, indicating no significant enhancement of Zn in fs LA of a brass alloy. These results are in agreement with the measurements of the aerosol composition in ns and fs ablation of brass alloys using low-pressure impaction [23].

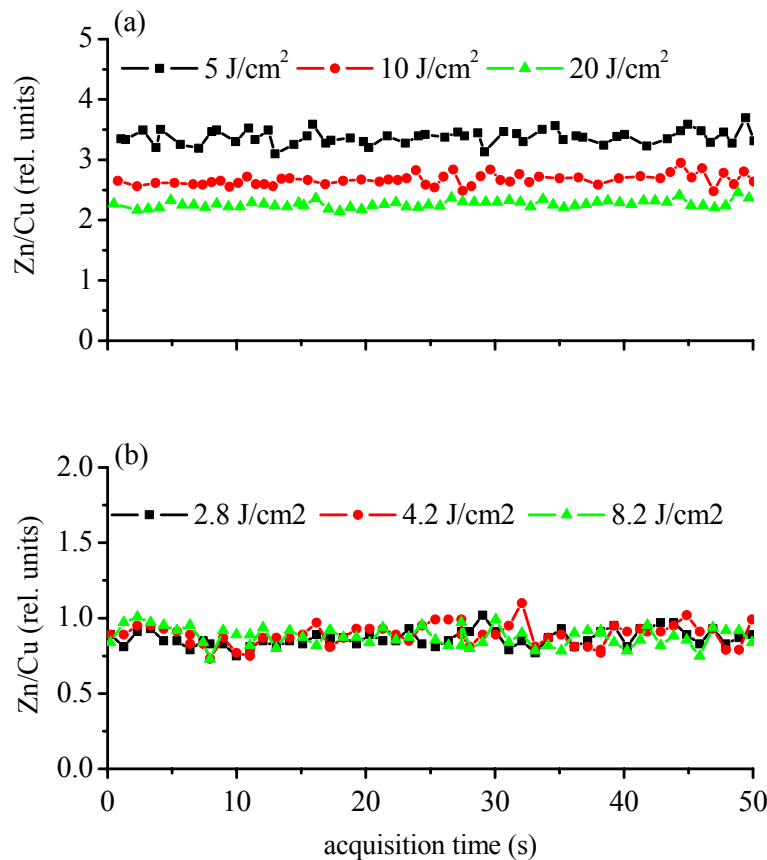
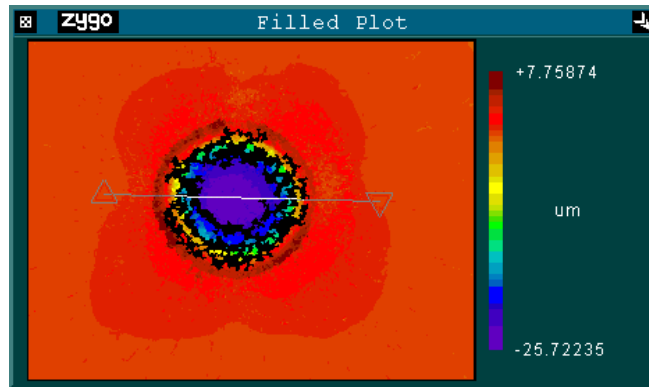


Figure 3.1 Transient Zn/Cu intensity ratio profiles in ablation of brass TD-07 at different fluences.

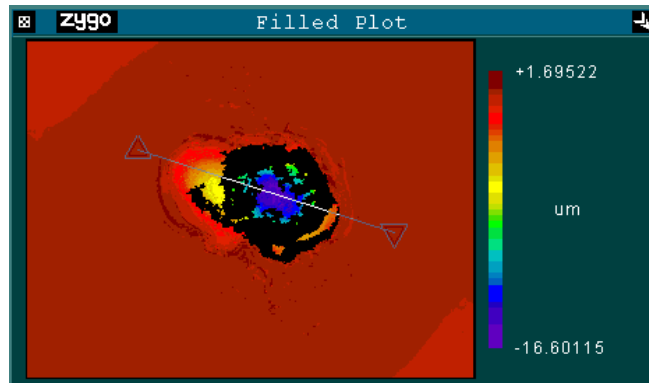
(a) Nanosecond laser ablation and (b) Femtosecond laser ablation.

3.2 Analysis of femtosecond laser-irradiated region

The ablation crater is associated with the laser irradiance and the optical, and thermal properties of a material. Nanosecond laser ablation produces a raised rim along the crater perimeter, which is caused by ejection and resolidification of molten material [49]. In contrast, melting and splashing could be reduced using femtosecond laser pulses. There should be also no elevated rim around the crater [50]. However, the properties of the material can affect the process of laser-matter interaction, providing a variation of crater shapes and ablation efficiency even with femtosecond laser ablation.



(a)



(b)

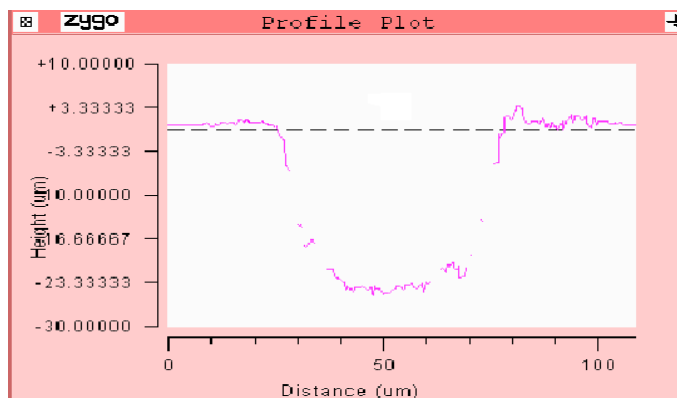
Figure 3.2 White-light interferometric microscope images of craters in fs ablation of (a) brass TD-07 and (b) NIST 610 Glass by 20 laser shots. (The color code of the depth is shown at the right side of the plots. The cross-sectional profiles between the two triangles are shown in Fig. 3.3)

Brass TD-07 and NIST 610 Glass, representing metallic and dielectric materials, were ablated using the femtosecond laser (fluence of 42 J/cm^2). The craters created by 20 laser

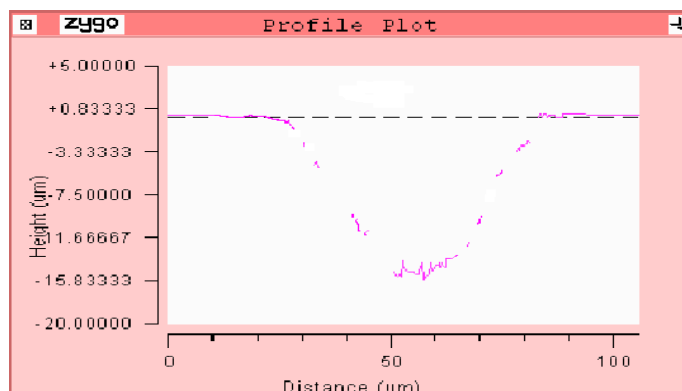
shots were measured with a white-light interferometric microscope (Zygo, New View 5010). The images and the cross-sectional profiles are shown in Fig. 3.2 and Fig. 3.3, respectively.

Both crater shapes are round (Fig. 3.2). The different colors represent the depth of the crater, and the black color shows the parts that could not be measured because of the low reflection.

Using a laser beam with a Gaussian profile, the shape of an ablation crater in glass is cone-like (Fig. 3.3 (b)). However, it is more like a crater with a straight wall for brass (Fig. 3.3 (a)). The crater volume in the brass sample is much bigger than that in the glass sample. The crater diameter in brass was 30 % larger than the crater diameter in glass after 300 shots ablation. Therefore, an internal standard method is necessary for quantitative elemental analyses of solid samples. The internal standardization avoids the different sampling quantities between samples and standards.



(a)



(b)

Figure 3.3 Profiles of the craters produced by fs ablation of (a) brass TD-07 and (b) NIST 610 Glass. 20 shots were applied in both cases.

Chapter 4

Femtosecond LA-ICP-OES

Laser ablation inductively coupled plasma (LA-ICP) spectrometry has been proven to be a powerful technique for the comprehensive, semi-quantitative analysis of solid matter [51-53]. However, non-accurate quantification as a result of elemental fractionation has recently been identified as one of the most crucial aspects preventing LA-ICP spectrometry to achieve more acceptance as an alternative to well established methods such as solution nebulization (SN) ICP-OES/MS.

In the ideal case, the sample material evaporated by the laser should (i) represent the exact bulk composition, (ii) be converted into an aerosol that can be transported to the detector site without losses [48, 54], and (iii) be completely decomposed within the ICP source [55, 56].

In contrast to ns-lasers, ultra-short pulse lasers could improve the ablation characteristics and get closer to the ideal of stoichiometric sampling due to the suppression of thermal effects [26, 21]. Applying a laser pulse of about 200 fs duration, ultra-fine aerosols have been produced from brass alloys at fluences below 5 J/cm^2 . These aerosols can be carried without significant losses to the ICP. They are so fine that complete evaporation can be expected. As a result the measured Zn/Cu ratios should reflect the compositions of the bulk material. With a shorter pulse (100 fs), stoichiometric aerosols could be obtained from brass alloys even for fluences up to 50 J/cm^2 [57]. Similar characteristics have also been observed for fs LA of dielectric samples [58].

In this chapter, the strategies of non-matrix matched calibration in fs LA-ICP-OES are investigated. Aerosols produced by ablation of various brass, Al, and silicate glass samples have been analysed for Zn and Cu.

4.1 Experimental

The femtosecond laser and the ICP-OES instrument have been described in Chapter 2. To avoid a plasma breakdown above the sample, the focus position was set 1 mm below the sample surface. Taking into account the $1/e^2$ criterion, the beam diameter at the sample surface was determined to be about 100 μm . The fluences given below refer to peak rather than to average values. The laser energy and the fluence could be adjusted using an attenuator consisting of a retardation plate and a thin plate polarizer. A flow rate of 0.8 L/min He was applied to transport the aerosol particles out of the cell. Right behind the cell outlet an additional amount of 0.12 L/min Ar was admixed, which enabled to reduce the background noise by a factor of about two.

Table 4.1 Instrumentation and experimental conditions applied for ICP-OES

ICP-OES / Data acquisition	
RF power	1350 W
Carrier gas	0.8 L/min He + 0.12 L/min Ar
Auxiliary gas	1.5 L/min Ar
Time per slice	1 s
Signal increment	10 %
ICP volume imaged onto spectrometer slit	
Cross section [#]	$\approx 1.0 \text{ mm}^2$
Depth of focus [#]	$\approx 10 \text{ mm}$

[#]Approximate values given by the manufacturer

Zn and Cu analyses of aerosols have been accomplished using the ICP-OES with conditions listed in Table 4.1. The instrument is designed to observe the plasma emission end-on. Therefore, element-specific responses should reflect the aerosol composition provided that injected particles are completely decomposed and element-dependent diffusion of eroded matter out of the plasma axis can be disregarded. In contrast, side-on

observation has to be assumed as more susceptible to non-representative responses since it requires complete isotropy of the analyte distribution in both axial and radial direction. The benefits of end- compared to side-on detection are discussed by Mermet [4, 59]. It has to be noted that no modifications were made on the optical layout of the instrument used. For instruments with other optical properties, however, an adaptation might be needed if the volume that is imaged onto the entrance slit of the monochromator collects an undersized part of the injection channel of the ICP.

The results documented exclusively refer to Zn and Cu as major or minor matrix constituents. In most cases, the neighboring ionic lines at Zn 202 nm and Cu 224 nm were chosen as analyte lines in order to avoid errors due to self-absorption caused by high element concentrations. Of course, these lines provide lower sensitivity than the most prominent line emission at 213 nm (Zn) and 324 nm (Cu) which should be used if Zn and Cu are trace elements.

Three randomly selected spots on the surface of each sample were ablated. Data reported here are averaged values. The compositions of the metal and glass standards used are given in Table 2.2.

4.2 Comparison of transient Zn and Cu signals

In Fig. 4.1 the transient Zn and Cu signals from the TD-07 brass sample are shown. The ablation frequency was 10 Hz and three different fluences were applied. The signal intensities varied depending on the fluence set. While the responses for 0.8 and 2.6 J/cm² were smooth, signals acquired at 8.2 J/cm² became more noisy but no spiking occurred. Furthermore, a direct comparison between the Zn and Cu signals revealed a strong correlation. In contrast, signals acquired for the Al sample AW-3414 tend to diverge at fluences below 5 J/cm², as can be seen in Fig. 4.2. Moreover, the reproducibility obtained in this case turned out to be bad.

LA of silicate glasses resulted in smaller signal intensities at the same experimental conditions. This is due to the higher transparency of the sample in the NIR spectral range which significantly affected the ablation threshold and lowered the total amount of material ablated per spot. In fact, the application of a Gaussian-type, i.e. non-

homogenized, laser beam leads to the formation of cone-like craters, as shown in Fig. 3.3. The pulse energy is therefore spread over a continuously growing area which means that the fluence is getting smaller during ablation, eventually falling below the threshold. Consequently, elemental responses were found to experience a more rapid decrease compared with those recorded for the metal standards. In Fig. 4.3, the Zn and Cu responses measured for the glass standard no. 3 with 2.6, 5.0, and 11.0 J/cm² are shown. As can be seen, the signal widths varied from about 10 up to 50 s, depending on the fluence applied. It should be stressed, that the plots shown in Fig. 4.3 refer to the atomic emission at Zn 213 and Cu 324 nm.

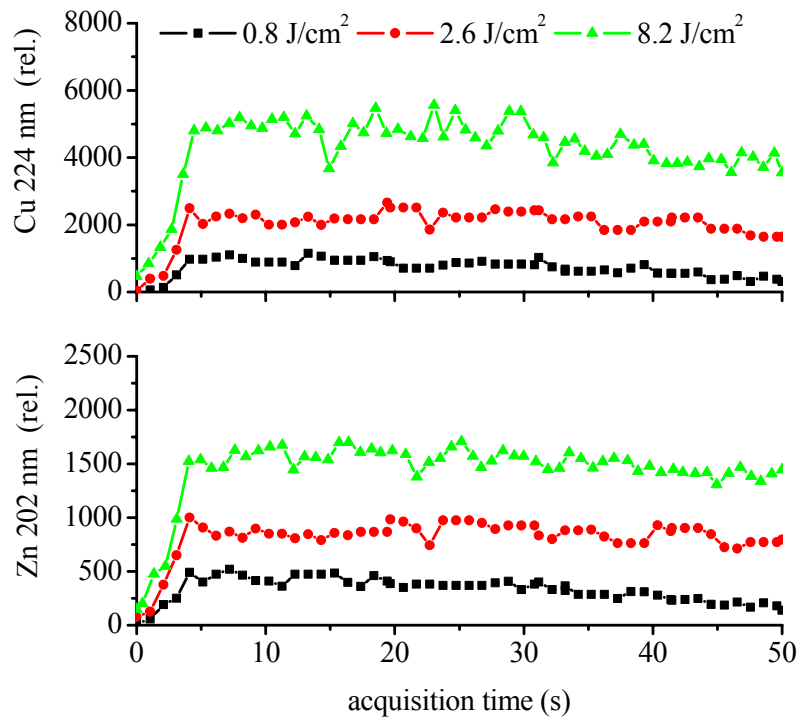


Figure 4.1 Transient Zn and Cu signals of brass TD-07 using near-IR fs LA at 10 Hz for three different fluences up to 8.2 J/cm².

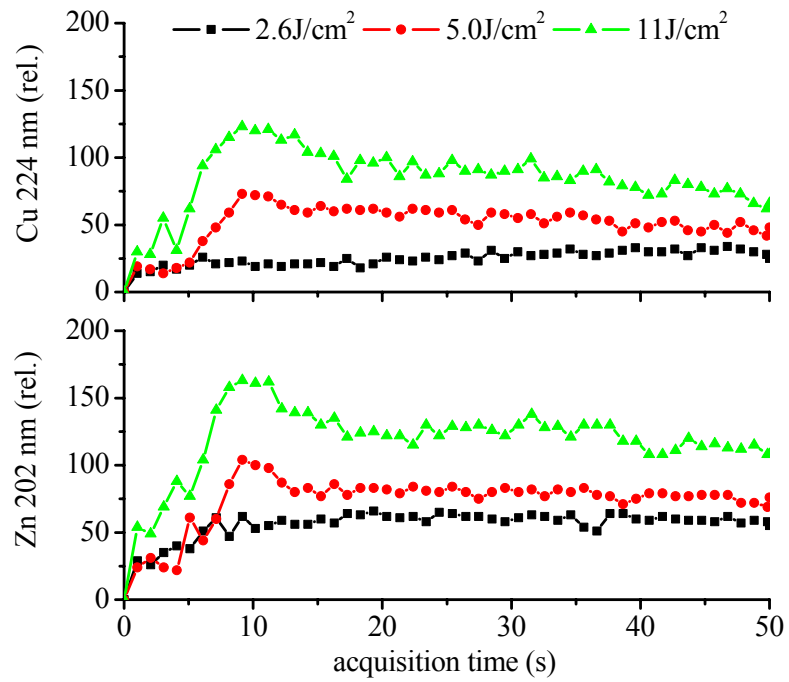


Figure 4.2 Transient Zn and Cu signals of Al AZ-3 using near-IR fs LA at 10 Hz for three different fluences up to 11.0 J/cm².

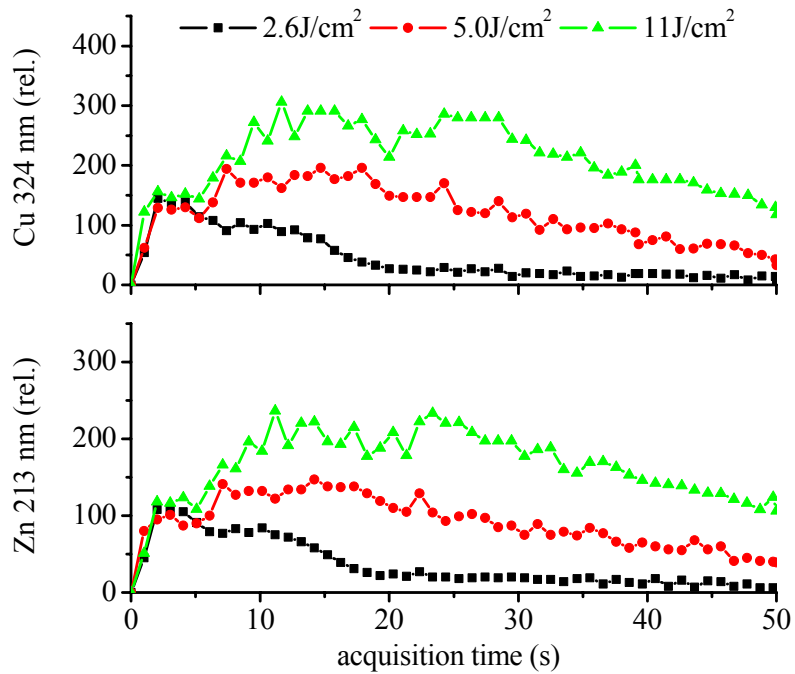


Figure 4.3 Transient Zn and Cu signals of silicate glass no. 3 using near-IR fs LA at 10 Hz for three different fluences up to 11.0 J/cm².

4.3 The dependence of the Zn/Cu ratio on time and fluence

Apparently, the determination of the Zn/Cu ratio from the integral values according to

$$\frac{Zn}{Cu} = \frac{\int_{t_1}^{t_2} r_{Zn}(t) dt}{\int_{t_1}^{t_2} r_{Cu}(t) dt}, \quad (4.1)$$

comprehends all information relevant to identify potential differences of measured and certified sample compositions. Here, r_{Zn} denotes the Zn- and r_{Cu} the Cu-specific response. However, the elemental ratio has been determined incrementally using

$$\frac{Zn}{Cu} = \frac{\int_{t_1}^{t_2} r_{Zn}(t) dt}{\int_{t_1}^{t_2} r_{Cu}(t) dt} \cdot \Delta t, \quad (4.2)$$

in order to visualize the temporal dependence. Please note, that both expressions are only equal if the elemental responses are proportional to each other ($r_{Zn} \propto r_{Cu}$). Discrepancies of expressions (4.1) and (4.2) would therefore directly indicate fractionation.

The time-dependence of the Zn/Cu ratio calculated for brass TD-07 applying 0.8, 8.2, and 11.0 J/cm² is exemplarily depicted in part (a) of Fig. 4.4. Due to the proportional changes of the Zn and Cu responses (e.g., shown in Fig. 4.1), a nearly constant ratio of approximately 0.4 was obtained for fluences larger than 0.8 J/cm². During the first seconds, however, the Zn/Cu ratio strongly fluctuated indicating pronounced fractionation, probably as a result of insufficient evaporation of micrometer particles within the ICP. Large particles are known to be formed in the initial stage of the ablation cycle [60]. Furthermore, the mean Zn/Cu value was found to increase by more than 30 %, most likely because of preferential evaporation over the entire period of analysis. These findings were found to apply to all brass standards used.

For Al, the fluence-dependence of the Zn/Cu ratio followed a similar trend as in the brass measurements. The results are shown in part (b) of Fig. 4.4. However, the threshold for non-fractionated evaporation apparently shifted towards a fluence beyond 2.6 J/cm² because of the higher formation enthalpy of Al. In contrast, responses measured for the silicate glasses (see part (c) of Fig. 4.4) lead to an almost constant Zn/Cu ratio for fluences between 2.6 and 11.0 J/cm². It should be emphasized, that a threshold-close

analysis was not made due to the small ablation rate mentioned above. At 2.6 J/cm^2 , the Zn/Cu ratio became noisy for $t > 20 \text{ s}$ due to the decreasing signal intensity.

The dependence of the Zn/Cu ratio on the fluence is shown in Fig. 4.5 for a brass, an Al and a glass sample. For better presentation, the Zn/Cu ratios of the three samples were normalized for the values measured at 11.0 J/cm^2 . As can be seen, the ratios measured in brass and Al varied up to a fluence of about 5 J/cm^2 , whereas the Zn/Cu ratio for silicate glass was independent of the fluence. Beyond 5.0 J/cm^2 , all values converge indicating the formation of stoichiometric aerosols.

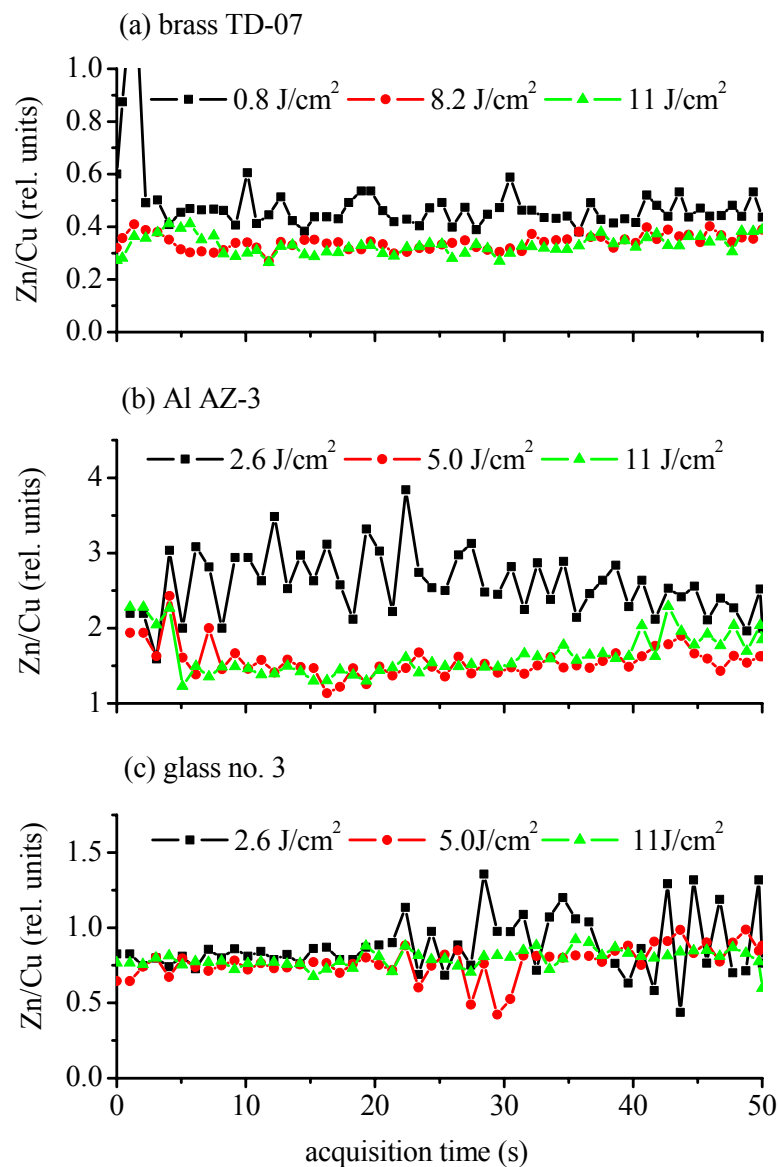


Figure 4.4 Transient Zn/Cu ratios for brass TD-07, Al AZ-3, and silicate glass no. 3 at different laser fluences.

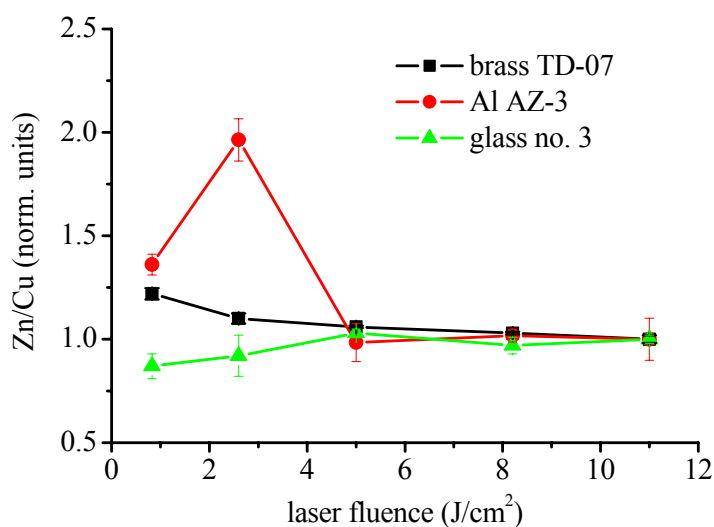


Figure 4.5 Fluence-dependence of the Zn/Cu ratio for three selected metal and glass samples.

For better representation, the values were normalized to the data points determined at the fluence of 11.0 J/cm².

4.4 Non-matrix matched calibration

In order to prove the hypothesis of matrix-independent analysis for fluences > 5 J/cm², the linearity of calibration graphs was examined. For this purpose, the Zn/Cu ratios of five brasses and two Al samples were plotted against their corresponding concentration ratios applying fluences between 0.8 and 11.0 J/cm². The Zn/Cu intensity ratios were measured taking into account an analysis time of 30 s. According to the results shown in Fig. 4.6, linear calibration curves could only be obtained for fluences larger than 5 J/cm², which are consistent with the data documented above. The correlation coefficients varied from 0.96 for 2.6 J/cm² up to 0.999 for 11 J/cm². Considering only brass, however, the slope of the calibration plots was found to be constant for fluences larger than 2.6 J/cm², as shown in the insert of Fig. 4.6. Nevertheless, the application of fluences significantly above the ablation threshold seems to favor the production of stoichiometric aerosols and should be applied for accurate analyses.

All Zn/Cu data obtained with the brass samples, Al and the glass samples at fluences larger than 5 J/cm² are also plotted in Fig. 4.7. The calibration shows an excellent

linearity throughout the fluence range considered. The correlation coefficients were found to be better than 0.999.

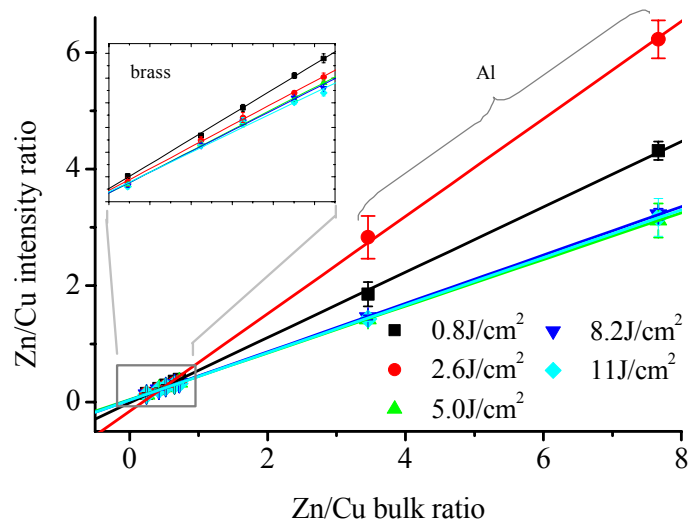


Figure 4.6 Calibration graphs taking into account the Zn and Cu responses measured for the brass and Al standards at different fluences.

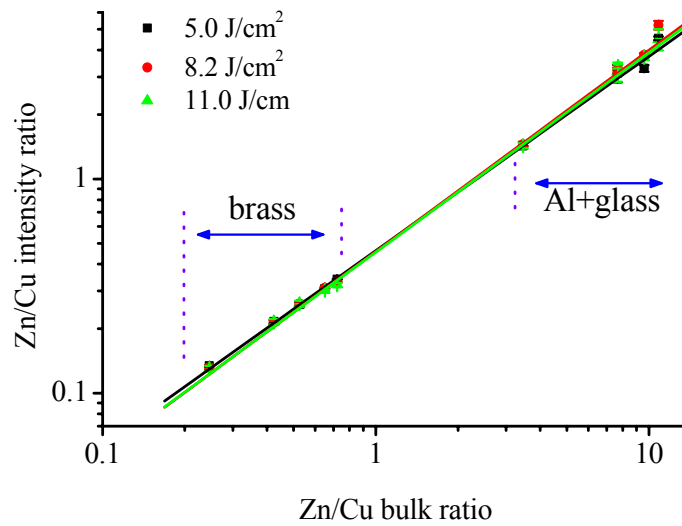


Figure 4.7 Calibration graphs taking into account the Zn and Cu responses obtained for brass, Al, and glass at 5.0, 8.2, and 11.0 J/cm².

4.5 Summary

The prospects of fs LA-ICP-OES for the accurate, non-matrix matched analysis of solid samples have been investigated. Three sets of different metallic and dielectric standards have been analyzed. It has been found that the Zn and Cu signals and corresponding Zn/Cu ratio tend to systematically stabilize for fluences from 2.5 to 5 J/cm², depending on the material considered. Threshold-close fluences, however, resulted in less reproducible and noisy responses, in particular, for Al. Furthermore, the Zn/Cu ratio measured for brass and Al slightly increased suggesting preferential evaporation of Zn during ablation. However, LA beyond a fluence of 5 J/cm² resulted in linear, matrix-independent calibration graphs. The data documented imply that fs LA-ICP-OES using fluences far above the ablation threshold efficiently suppresses fractionation and allows to perform accurate, non-matrix matched analyses.

Chapter 5

Femtosecond LA-ICP-MS

ICP-MS is a widely used analytical method for elemental analyses due to its high sensitivity, wide dynamic range and relatively simple spectra. The main difference, compared with ICP-OES in axial viewing mode, is that the analytes (ions) are extracted locally from the plasma via a sampler [61].

This ion extraction mode is successful in elemental analysis using solution nebulization (SN) ICP-MS because all aerosols transported to an ICP have the same compositions independent of their sizes. Therefore, the relative signals of elements should be independent of the sampler positions [62, 63].

However, solid analyses using LA-ICP-MS are different because LA typically produces particles with size-dependent chemical composition. The locations in an ICP where vaporization, atomization and ionization occur are related to the elemental thermal volatilities and the particle sizes. Large particles require a longer residence time than small ones to undergo the various processes. Therefore, large-sized particles are atomized further downstream [64]. The generated ions from different element atoms are nonuniformly and widely distributed in an ICP.

Femtosecond lasers produce ultrafine aerosols. The potential of accurate, non-matrix matched analysis of solids using fs LA-ICP-OES has been verified in Chapter 4. This analysis using LA-ICP-MS should consider the effect of ion distributions in an ICP. Therefore, the ion distributions in the ICP for different matrices are investigated using fs LA-ICP-MS.

5.1 Experimental

The femtosecond laser, the ablation unit and the ICP-MS instrument have been described in Chapter 2. The focus position of the laser beam was set 0.5 mm below the sample surface. The plasma torch box was mounted on an X-Y-Z translation stage. Thus, it was easy to scan the plasma along axial and radial directions. The operation conditions are shown in Table 5.1. Differently from LA-ICP-OES, the central gas flow rate was 1.5 L/min. With this flow rate, the mixed gases (argon and helium) were capable of penetrating the boundary layer in front of the sampler orifice. The use of helium gas (the gas in the ablation cell), however, was found to cause degradation of the analyzer pressure. It resulted in a high background and low sensitivity in elemental analysis. Therefore, sampler and skimmer cones with small sized apertures were used.

Table 5.1 Experimental conditions for ICP-MS

RF power	1400 W
Reflected power	8 W
Plasma gas	16 L/min
Auxiliary gas	2.2 L/min
Argon (behind the ablation cell)	0.65 L/min
Helium (before the ablation cell)	0.83 L/min
Sampler cone/skimmer cone	Ni 0.7 mm/0.5 mm
Torch size (outer /middle /injector tube)	18/16/1.5 mm
Dwell time	10.24 ms

5.2 Axial and radial ion distributions in the ICP

The axial ion signals were detected along the central axis of the ICP, while the radial ion signals were recorded along the radial direction at a fixed sampling depth. Three measurements were made at each location in the ICP. 100-s transient signals were collected, but the first 10-s signals were excluded in calculation of the ion intensities.

Axial ion signals were obtained in fs LA of brass TD-07 at a laser fluence of 35 J/cm². Fig. 5.1 shows the ⁶⁴Zn and ⁶³Cu signal intensities with the sampling depths (distance

between the sampler tip and the nearest load coil) from 9 mm to 16 mm. The signal intensities increased when the sampling depth was changed from 9 mm to 12 mm. Both ^{64}Zn and ^{63}Cu signals reached their maximum values at a position of 12 mm where the ionisation was best. Only small quantities of ions were detected at the plasma tail.

Fig. 5.2 shows the $^{64}\text{Zn}/^{63}\text{Cu}$ ratios at on-axis positions in the ICP. The ratios decreased by about 27 % when sampling depths were increased from 9 mm to 14 mm. Zn was preferentially ionized at lower sampling depths despite the higher ionization potential than Cu. The enhancement of Zn signal was depressed for sampling depths ≥ 14 mm, thus nearly constant Zn/Cu ratios were obtained.

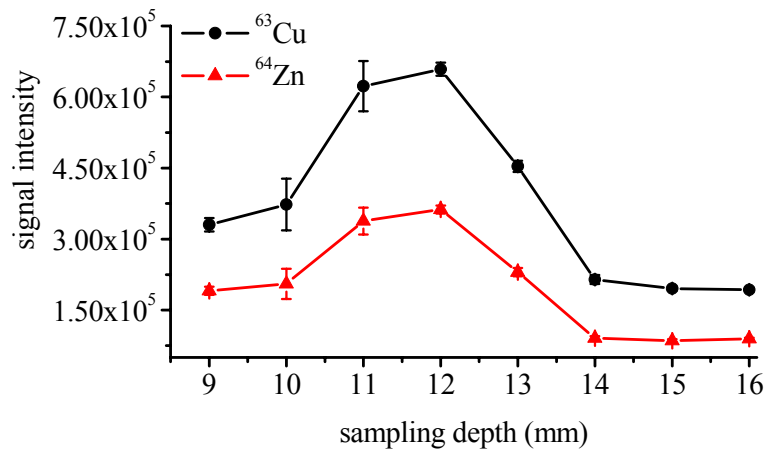


Figure 5.1 On-axis profiles of ^{64}Zn and ^{63}Cu signal intensities in ablation of brass TD-07.

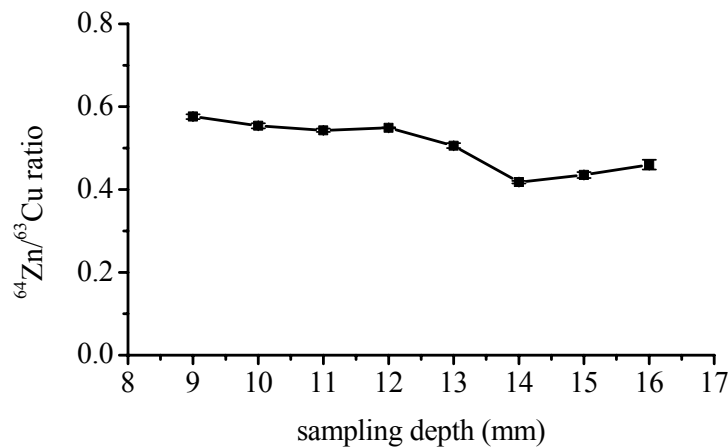


Figure 5.2 $^{64}\text{Zn}/^{63}\text{Cu}$ ratios in analysis of brass TD-07 at different sampling depths.

The radial ion distributions were investigated with brass and Al samples. The Zn and Cu ion signals were detected in the ICP along the radial direction at the optimum sampling depth of 12 mm. Fig. 5.3 shows the transient ^{64}Zn signals of brass TD-02 at radial positions from 0.3 mm to 1.6 mm. The signals in the center of the ICP are not shown because a different detection mode (analog mode) had to be used due to the strong signals. The signals decreased significantly from the central axis to a position of 0.5 mm off axis. The ion signals fluctuated significantly in comparison with the spectrum signals obtained by LA-ICP-OES. This reflects inhomogeneous ion distribution due to the localized evaporation of particles.

Fig. 5.4 shows the radial profile of Zn signals (●) in analysis of Al alloy VAW-3414. All signal intensities were normalized to the value in the central axis of the ICP. Large quantities of ions were located in the center of the ICP with a radius of 0.5 mm. In this experiment, a gas flow of 1.5 L/min was used to transport the aerosols to the plasma via an injector tube of 1.5 mm i.d.. Wider ion distributions along the radial direction were found when a lower gas flow rate and injector tubes with larger inner diameters were used.

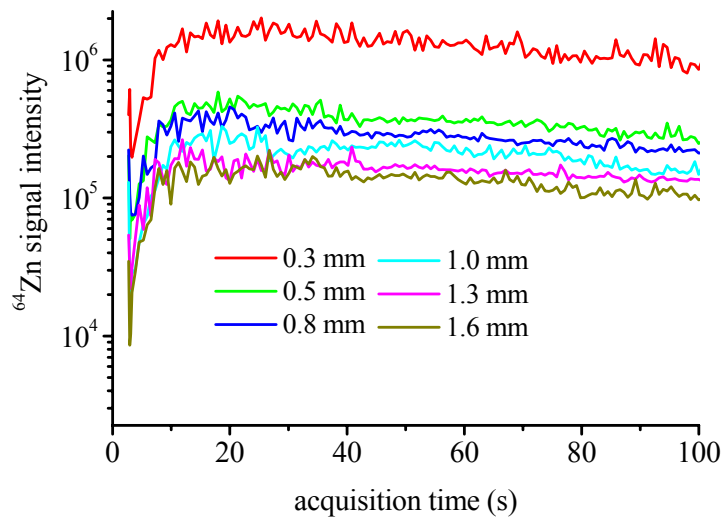


Figure 5.3 Comparison of transient ^{64}Zn signals at various radial positions of the plasma at sampling depth of 12 mm for the ablation of brass TD-02.

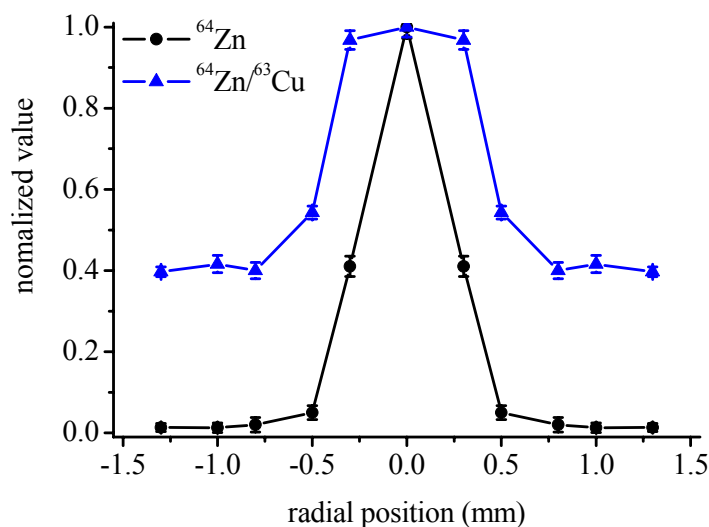


Figure 5.4 Normalized ^{64}Zn intensities (\bullet) and $^{64}\text{Zn}/^{63}\text{Cu}$ ratios (\blacktriangle) in ablation of Al alloy VAW-3414 at different radial positions within a plasma. (Sampling depth of 12 mm)

The normalized $^{64}\text{Zn}/^{63}\text{Cu}$ ratios at different radial positions are also shown in Fig. 5.4 (\blacktriangle). They were calculated from three measurements of the Al alloy VAW-3414. The maximum ratio was in the central axis of the plasma. The ratios decreased significantly from the central axis to 0.8 mm off axis, but they tended to be constant for positions ≥ 0.8 mm.

The ratio change is probably caused by size-dependent “digestion” of aerosols in the ICP. Femtosecond lasers produce ultra-fine aerosols in ablation of solids but a ratio deviation for different sized aerosols exists, e.g., small-sized particles are Zn-enriched and large-sized particles are Cu-enriched in ablation of brass alloy [23]. The degree of ionization of these particles depends on the atomization efficiency and the residence time of atoms in the ICP [60]. The temperature is lower within the central channel, because of the various processes taking place in this region (and thereby using energy) [1, 65]. Thus, the atomization process ended at a late stage when aerosols passed through this region. Incomplete consumption of big particles probably took place at the sampling depth of 12 mm. The surviving particles were enriched in the refractory species such as Cu. In contrast, when particles traveled through the region outside the central channel, high

ionization efficiency was obtained because the atomization process ended at an early stage.

5.3 Matrix effect on the Zn/Cu ratio

The matrix effect on the ratios at radial positions of the ICP was investigated since the ratio changed strongly in this direction. Gilding metal NBS 1113 (Zn/Cu: 0.050), brass alloy TD-07 (Zn/Cu: 0.72) and Al alloy VAW-3414 (Zn/Cu: 7.67) were analyzed for this purpose. The $^{64}\text{Zn}/^{63}\text{Cu}$ ratios vs. the radial positions within the ICP are shown in Fig. 5.5 (no signal ratio is shown for Al alloy at 1.6 mm because of the low response). Similar ratio changes can be found for these three metallic matrices.

In order to show the matrix effect clearly, the relative ratios between two matrices were calculated for each radial position (on-axis to 1.3 mm off-axis). Fig. 5.6 shows the relative ratios which are normalized by the values obtained in the center. The ratios for each pair of the three matrices fluctuated in a narrow range for the radial positions up to 1.3 mm. In fact, the ratio fluctuations reflect two effects. One is the aerosol size- and element-dependent ionization in the ICP, and the other is the effect of the matrix element (Cu, Zn or Al) on the plasma temperature and on the electron number density. The second effect is independent of the LA process.

The small matrix effect has also been verified by the acquisition of linear calibration curves at various radial positions. Fig. 5.7 shows the calibration curves of a series of brass standards with Zn/Cu ratios from 0.05 to 0.72. Despite the differences of the curve slopes at each radial position, the correlation coefficients of all curves were better than 0.995. Similarly, relatively linear calibration curves of two sets of brass and Al standards were also received (shown in Fig. 5.8).

The obtained results indicate that the aerosols ablated from different metallic matrices using fs lasers have similar size distributions. The ionization of these aerosols occurred in the same positions in the ICP. Therefore, accurate, non-matrix matched analyses of solids are also possible using fs LA-ICP-MS.

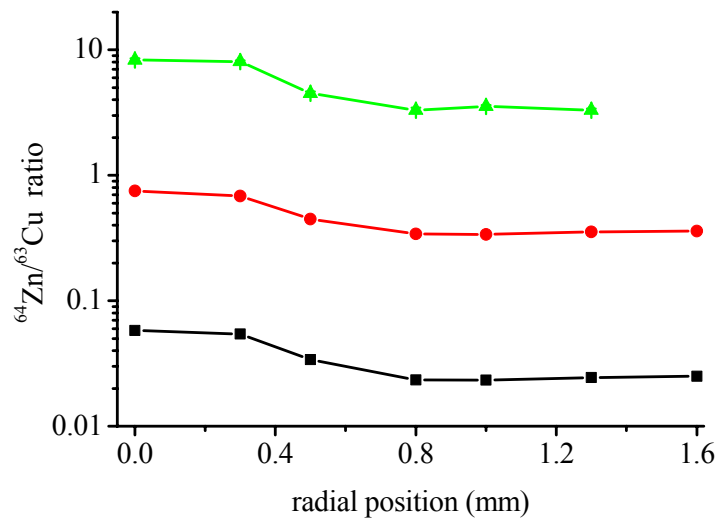


Figure 5.5 Comparison of $^{64}\text{Zn}/^{63}\text{Cu}$ ratios of three matrices at different radial positions within the plasma. (-▲- Al alloy VAW-3414, -●- Brass TD-07 and -■- Gilding metal NBS 1113)

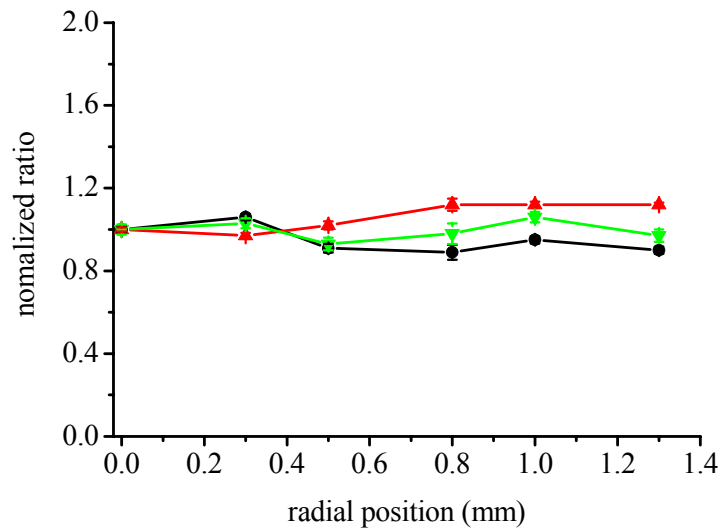


Figure 5.6 Profiles of normalized ratios between two samples at different radial positions within the plasma. (-▲- Brass TD-07/Gilding metal NBS 1113, -▼- Al alloy VAW-3414/Gilding metal NBS 1113 and -●- Al alloy VAW-3414/ Brass TD-07)

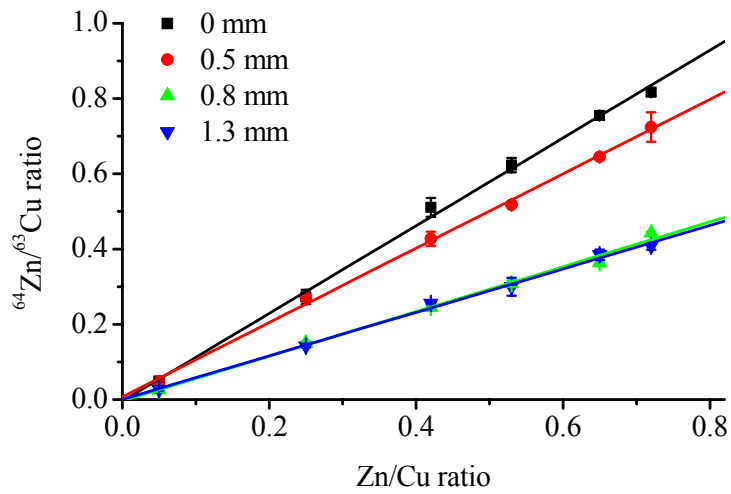


Figure 5.7 Calibration curves of a series of brass standards at four radial positions within the plasma. (Sampling depth of 12 mm)

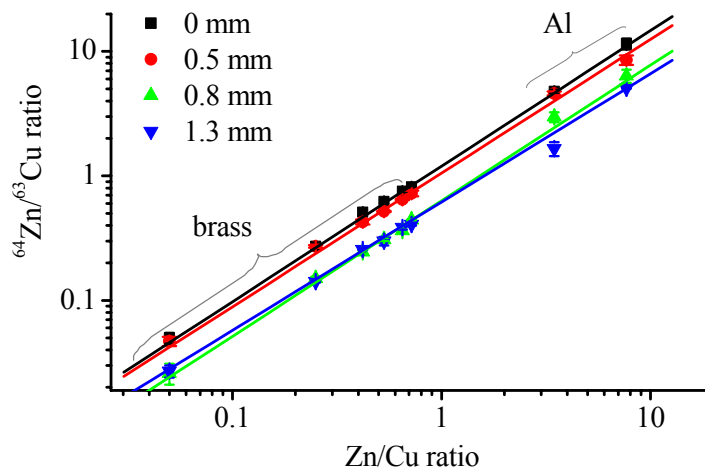


Figure 5.8 Calibration curves of brass and Al alloy standards at four radial positions within the plasma. (Sampling depth of 12 mm)

5.4 Laser fluence effects on the Zn/Cu ratio

The above investigation was based on the high laser fluence, but different laser fluences can affect the qualities of ablated aerosols. Moreover, silicate glasses cannot be analyzed at off-axis locations in the ICP because of the low concentrations of Zn and Cu.

Therefore, the laser fluence effects on Zn/Cu ratios of metals and silicate glasses were investigated at laser fluences between 2 and 34 J/cm². The Zn- and Cu-ion signals were recorded at the cross point of the central axis and the sampling depth of 12 mm in the ICP.

Fig. 5.9 shows the profiles of the ⁶⁴Zn/⁶³Cu ratios vs. laser fluences in ablation of five brass alloys and two Al alloys. Constant ratios were obtained in the fluence range investigated, indicating negligible fluence effect on ⁶⁴Zn/⁶³Cu ratios for the metallic samples at laser fluences far above the ablation threshold. In contrast to brass alloys, worse standard deviations on the basis of three measurements were found for Al alloys, in particular, at low fluences.

However, the ⁶⁴Zn/⁶³Cu ratios for silicate glasses were strongly fluence-dependent. Fig. 5.10 shows the normalized ⁶⁴Zn/⁶³Cu ratios for laser fluences between 2 and 34 J/cm². The ratios increased with the increase of the laser fluences for all samples, but the increase was significantly depending on the properties of silicate glasses. The ⁶⁴Zn/⁶³Cu ratio of NIST 610 Glass at 34 J/cm² was more than 8 times higher than that at 2 J/cm², while the change was less than 20% for glass no. 3.

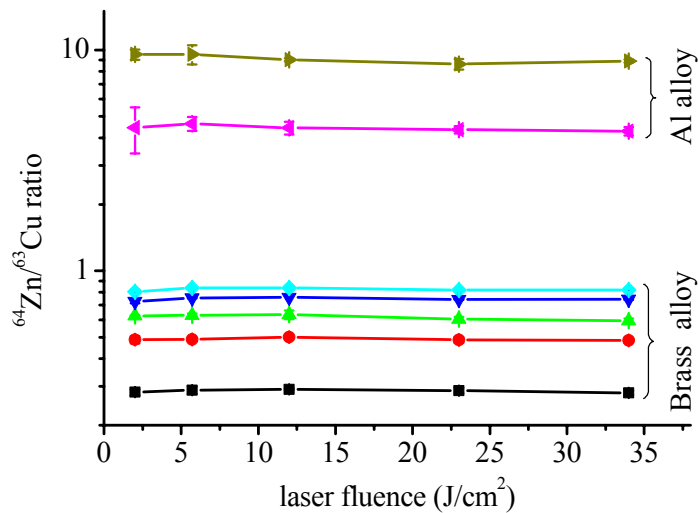


Figure 5.9 ⁶⁴Zn/⁶³Cu ratios measured at different laser fluences in ablation of brass and Al alloys.

(Brass: -■- TD-02, -●- TD-03, -▲- TD-04, -▼- TD-06, -◆- TD-07 and
Al: -◀- AZ-3, -▶- VAW-3414)

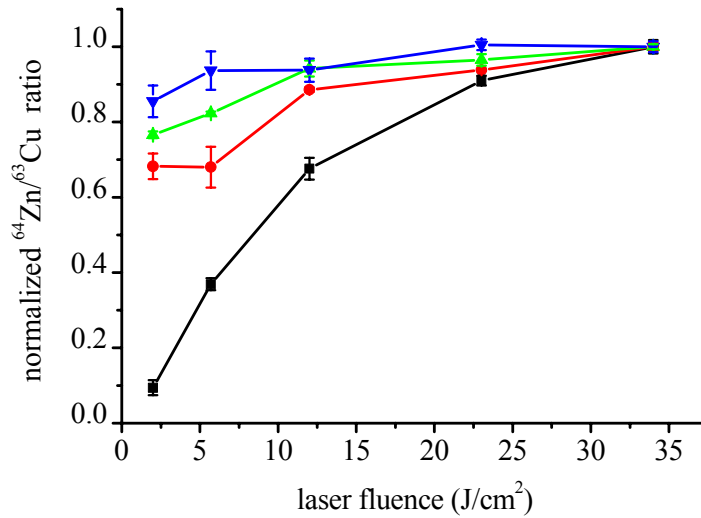


Figure 5.10 Normalized $^{64}\text{Zn}/^{63}\text{Cu}$ ratios at different laser fluences for four silicate glasses. (-■- light blue NIST 610, -●- brown glass no. 1, -▲- grey glass no. 2, -▼- dark glass no. 3)

5.5 Summary

The spatial distributions of Zn- and Cu-ions in the ICP have been investigated in fs laser ablation of brass- and Al-alloy materials. The ions were nonuniformly distributed in the ICP, but large quantities of ions were located in the center. Zn/Cu ratios changed significantly along the radial direction at the sampling depth of 12 mm. However, matrix effects on Zn/Cu ratio were small with respect to the metallic materials investigated. The effects of laser fluences were negligible on the Zn/Cu ratios of brass and Al alloys, but the ratios of silicate glasses were significantly dependent on the laser fluences as well as the glass properties.

III. Flow digestion of solid sample

Chapter 6

Introduction of solid sample digestion

In this part of the thesis, another sample handling technique, flow digestion of biological and environmental powders, is investigated. Solid samples are commonly digested to form solutions for introduction applying a nebulization method. Some methods used for solid digestion are listed in the figure shown in the Introduction. The basic digestion procedure involves the addition of suitable reagents (e.g. acids, melting reagents) to the sample and enough energy to break bonds or to destroy the crystalline structure of solids. Two basic procedures are normally utilized for solid sample preparation: dry decomposition and wet digestion.

Dry decomposition

Dry decomposition by fluxes (fusion) is normally used for refractory materials, mineral oxides and iron alloys. Dry ashing is usually performed by thermal decomposition of organic compound and extracting mineral elements from the residua using acid [66]. The major advantages of dry decomposition are relative safety and the ability to decompose large sized samples. The main disadvantages are expenditure of time and the loss of volatile elements. Thus, it is considered more of a “last resort” for sample treatment.

Wet digestion

In contrast, wet digestion is a widely used sample preparation method, whose benefit over dry decomposition is speed. Various digestion techniques using atmospheric or elevated pressure with thermal or radiant source have been developed. Biological and environmental samples consist mainly of organic matter with mineral components. For digestion of these important samples, oxidizing acids are usually used at high temperatures. Nitric acid is the most often used oxidant, but for samples with silicates, additional hydrofluoric acid is necessary.

Open digestion systems: Sample digestion at atmospheric pressure with an open vessel is undoubtedly the simplest method. A conventional approach is to apply heat from a Bunsen burner, heating plate, sand bath, etc., operating either at certain temperature or in a response to a temperature program. This technique is of great value for routine analyses because many samples can easily be handled simultaneously. The limitation is its low digestion temperature, which depends on the ambient-pressure boiling point of the corresponding acid, e.g., the boiling point of nitric acid is 122 °C. At such low temperature, the oxidizing power of nitric acid with respect to biological and environmental samples is insufficient. One possible remedy is to use a mixture of high boiling point acids (sulfuric, perchloric and nitric acids) as digestion reagent to increase the temperature of a digestion. Sample digestion in an open system still consumes lots of time and a large quantity of reagents; even so, some samples are generally not subject to complete digestion. Other disadvantages relate to the risk of contamination from environment, the danger of losses of volatile elements, and the need of constant supervision.

Closed digestion systems: When two chemicals react, their molecules have to collide with sufficient energy (activation energy). Elevating the reaction temperature brings about higher energy and more collisions, which result in a faster chemical reaction rate. The relationship between the chemical reaction rate and the temperature is determined quantitatively by the Arrhenius equation [67]

$$k = A \exp\left(-\frac{E_a}{RT}\right), \quad 6.1$$

where k is the rate coefficient, A a constant, E_a the activation energy, R the universal gas constant, and T the temperature (in degrees Kelvin). In accordance with this equation, the reaction rate is approximately doubled depending on the activation energy when the temperature is increased by 10 K. Furthermore, the oxidation power of a digestion reagent shows strong dependence on temperature [1]. Thus, oxidizing acids are usually used at temperatures as high as possible.

In order to increase the digestion temperature, closed vessels have been applied. The relatively high temperature is obtained due to the rise of the reagent boiling point at a high pressure. Under the elevated temperature condition, complete sample digestion becomes possible in a short time. Other advantages of closed systems involve minimizing contamination and no loss of volatile elements. The pressure itself is, in fact, nothing more than an undesirable but unavoidable side effect.

The first method for sample digestion under elevated temperature and pressure was performed by Carius in 19th century in a sealed glass tube [66]. With Carius' technique, a temperature between 250 to 300 °C was obtained with an internal pressure of more than 100 bar. However, extreme care should be taken during heating because of the risk of explosion. Based on this technique, the method of closed vessel digestion has been developed.

In 1960, the manufacture techniques of organic polymers made much progress, resulting in the development of a pressurized digestion vessel with PTFE (polytetrafluoroethylene) or PFA (perfluoroalkoxy) [66]. Using such kind of vessels, the digestion temperature can be raised by electric heating to values as high as 200 °C in the conventional heating mode [68]. However, much time was spent on preheating and cooling the vessel due to the thermal convection process.

A significant advance in sample digestion was achieved by the development of microwave technology [17, 18]. Microwave digestion systems facilitate the direct heating of the sample without heat-transfer through the surrounding material, thus microwave digestion is more efficient than conventional heating means. In 1975, Abu-Samra et al. reported the first application of microwave-assisted digestion of biological samples [69]. In the 1980s, the closed vessels specially designed for microwave digestions succeeded in achieving a pressure up to 20 atm with an outer jacket [70].

In order to avoid the limited mechanical resistance of PTFE and PFA at high temperatures, the quartz vessel was used again in the digestion system [6]. The introduction of “high-pressure ashing” (HPA) by Knapp currently represents the leading technique in pressurized sample digestion [71-73]. The vessel is inserted in a heating block and balanced by adding an external pressure roughly equivalent to or higher than that formed inside. Therefore, the risk of explosion can be avoided even if the system works at temperatures and pressures up to 320 °C and 130 bar, respectively.

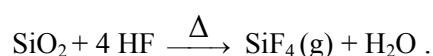
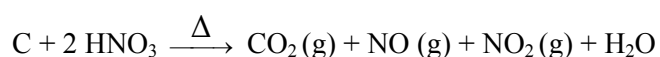
Flow digestion systems: Discrete digestions of solid samples at high or at atmospheric pressure require multi-step, labour-intensive and time-consuming procedures. Therefore, there is a demand of developing automatic systems for solid sample digestion. Digestion in a flow mode is becoming popular, because of its speedy and easy operation, small sample volume and the possibility of fully automated online analysis. Moreover, the continuous carrier stream flowing through the capillary can clean the whole system, avoiding a tedious vessel clean-up procedure. Sample digestion in a flow digestion system is fulfilled when samples containing oxidization acids are pushed through a heated coil. Until now, several flow digestion systems have been developed.

The initial work in this field was reported by Burguera *et al.* [74]. The continuous sample digestion was accomplished in a glass coil heated by a microwave oven in combination with a flow injection system. The disadvantage of this method is that only liquid samples, such as serum or blood, which require mild digestion conditions can be completely digested. Solid sample digestion requires “robust” flow systems because high temperatures are necessary for decomposition of organic matrices in a short residence time. The performance of the digestion system has been improved by heating a PTFE tube with either microwave oven [75] or a resistively heated oven [76]. The potential of the systems was demonstrated in digestion of various solid samples such as chocolate, sewage sludge, tomato leaves and cocoa powder. By using PTFE or PFA tubing, the maximum digestion temperature was restricted to 210 °C. Then new designs have been developed to reach higher temperatures. One way was to wrap the tube using a plastic tape with high mechanical strength [77]; another method was adding an external counter-pressure on the PTFE tube to maintain pressure equilibrium [73, 78]. With these designs, the equipments were able to reach a temperature up to 250 °C.

However, a temperature of at least 300 °C is necessary for complete digestion of organic compounds with nitric acid [24]. The further development of microwave-assisted digestion system depends on the invention of new materials with both microwave-transparent character and strong mechanical resistance.

The advantage of microwave heating over conventional electric heating in a flow digestion system is not obvious compared to that in a closed system. The limitation of capillary material using electric heating is greatly reduced. Compared to the capillaries made from glass and PTFE, Pt/Ir capillary exhibits excellent performance in withstanding high temperature, high pressure and concentrated acids [79, 80]. An alternative design with conventional electrical heating mode has been developed at ISAS [81]. A flow digestion system with an electrically heated Pt/Ir capillary could operate at temperatures up to 360 °C and pressures up to 30 MPa by using a restrictor capillary of appropriate length. The glass-free design of the digestion system permits the use of hydrofluoric acid that can improve the digestion of samples containing silicate.

A flow digestion system can be used in an off-line as well as in an on-line mode. In an on-line mode, the digestion system is coupled with an elemental detection instrument for flow sample digestion and online element analyses. However, the gas effects should be considered for effective coupling between them. During the digestion process, large quantities of gaseous reaction products (CO₂, NO and NO₂, etc) are formed by the oxidation of biological and environmental samples in nitric acid. The general reaction mechanisms responsible for formation of gaseous decomposition products are



The direct coupling of this system to a flame-AAS spectrometer provided the means for online element determinations [82]. The formed gases do not interfere in measurements by flame AAS since CO₂ is the “natural” main constituent of the flame gases and the small amounts of NO_x are too diluted in the flame gas to affect the flame properties significantly. In contrast to flame AAS, a direct coupling to an ICP-based spectrometer is unsuccessful because of severe plasma interference by these gases. Removing the gases after digestion and before detection can solve the problem.

Haiber et al. [81] used a combination of ultrasonic nebulizer and membrane desolvator as an interface for efficient gas removal. S.Wu et al. [83] applied a similar interface coupled to an ICP-MS spectrometer for use with microwave-assisted digestions of food and plant material, whereas Recknagel et al. [84] and M. de la Guardia et al. [85] employed a homemade liquid/gas separator (“bubble trap”), originally used in a hydride generation system, for the removal of the disturbing gases. Each of these interfaces has some disadvantages, such as large financial expense, large dead volumes, or time-consuming gas removal.

A further possibility for gas/liquid separation is the application of commercially available permeable membranes and tubing made of various materials with different specifications. There are numerous applications for such membranes in the field of chemistry, especially in flow injection analysis (FIA) systems [86.- 90]. For example, thin non-porous silicone membranes are chemically resistant to the acids used for digestion and are highly permeable for gases. Porous ceramics are also chemically resistant and their use is widespread in technical applications. In addition, porous membranes made of various plastics are commonly used.

In this part, a high-temperature/high pressure flow digestion system with electrically heated Pt/Ir or Ta capillary has been set up. The performance of the system in solid sample digestion is studied in detail. Various gas-permeable tubes for degassing of the digested solution are investigated with regard to chemical resistance, gas removal efficiency, and bubble point (the pressure at which a breakthrough of liquid occurs). By optimization, a simple and efficient gas removal interface is developed for the coupling of the digestion system with the ICP-OES.

Chapter 7

Instrumentation

This chapter presents the instruments that were used in the experiments. The whole on-line system includes a high-temperature/high-pressure sample digestion unit and detection instruments.

7.1 Flow digestion system and gas removal interface

Fig. 7.1 shows a schematic arrangement of the high-temperature/high-pressure (HTHP) flow digestion system, whose details are described below.

The digestion system consists of a standard HPLC pump with a titanium head (Knauer, Berlin, Germany), two 1/8'' HPLC sample introduction valves (PEEK), the indirectly electrically heated digestion capillary (Pt/Ir, 80/20), standard HPLC material tubes (1/16'') and a restrictor capillary with 64 μm inner diameter. The flow resistance of this capillary guarantees a back pressure in the whole system, which is high enough (> 17 MPa) to avoid vaporization of the liquid. The core part of the digestion system is the heating block, whose design is considerably compact and safe, as shown in Fig. 7.2. In order to avoid particle deposition caused by gravity, the axis of the coiled digestion capillary is in a vertical position. The volume of the sample loop is 0.6 mL, nested in two split loops each filled with 2.5 M HNO_3 .

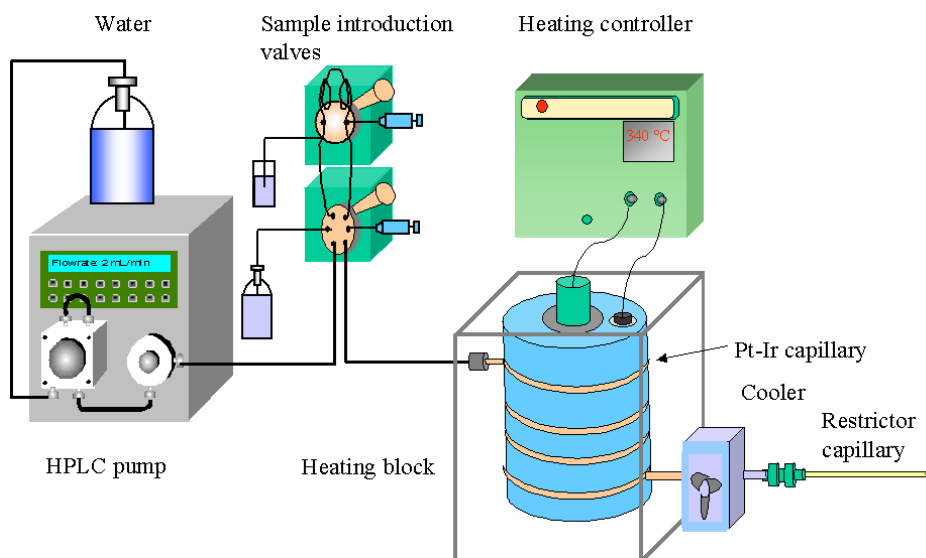


Figure 7.1 Schematic arrangement of the high-temperature/high-pressure digestion system.

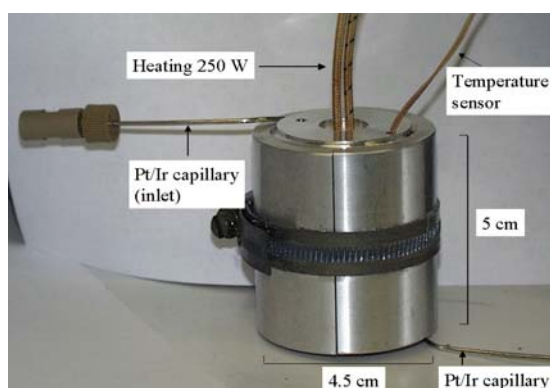


Figure 7.2 The heating block of the high-temperature/high-pressure flow digestion system.

Custom-made HPLC capillary (1.58 mm o.d., 1.0 mm i.d., length 150 cm) from a Pt-Ir alloy (80/20) was produced by drawing out a seamless Pt-Ir tube of larger diameter (Degussa, Frankfurt a.M., Germany). A 100 cm-length section of this capillary was heated. A capillary of tantalum (Ta) material was also used instead of Pt-Ir capillary for a comparison.

A homemade power supply (max. 400 W) equipped with a commercial PID controller (Horst, Lorsch, Germany) was used to supply power to a commercial cartridge heater (42 V, 250 W, 20 mm diameter, 50 mm length) positioned in the center of an aluminum cylinder (45 mm diameter, 50 mm height.). The Pt/Ir capillary is embedded in a milled groove of the aluminum cylinder and covered with heat-insulating glass wool and an aluminum shield.

The end piece of the Pt/Ir capillary outside the oven was embedded in the milled grooves of two jointed Cu plates (5 mm thick, 60 x 80 mm area), which were screwed onto a powerful commercial cooling unit equipped with cooling fins and a fan, normally used for microprocessors in personal computers (CPU cooler). This arrangement was sufficient to reduce the temperature of the digestion solution to below 40 °C even at flow rates up to 1.5 mL/min.

Polypropylene tubes have been applied for degassing of the solution. The dimensions of this tube are 2.7 o.d., 1.8 mm i.d., pore size 0.2 μm (bubble point: 0.32 MPa), up to 1 m length (Microdyne, Wuppertal Germany). A 1/16'' (1.58 mm) PEEK capillary with closed ends was inserted into the porous tube serving as an "inner rod", shown in Fig. 9.1(b). In order to enhance gas escaping through the tube wall, a short piece of PEEK capillary with small inner diameter was attached in front of the tube to increase the pressure inside the porous tube. The degassing tube is now fitted between two restrictor capillaries, as shown in Fig. 9.1(a). The first one (i.d. 64 μm) with a very high pressure drop delivers the necessary back-pressure for the sample digestion unit; the second one with a diameter of 130 μm and an appropriate length obtains a pressure drop of 10 kPa up to some hundreds of kPa.

7.2 ICP-OES and HG/CV-AAS

The ICP-OES instrument described in Chapter 2 (see Fig. 2.3) was coupled to the sample digestion system. This instrument, exclusively used in the axial observation mode, allows detection elements of interest.

After passing through a polypropylene tube, the gas-free solution was delivered to the nebulizer. A 12 cm-length capillary (130 μm i.d.) was connected between the polypropylene tube and the nebulizer.

Atomic absorption spectrometry (AAS) is still a widely used analytical technique for element determination [91]. Cold vapor (CV) or hydride generation (HG)-AAS is an ideal method for mercury and elements which form hydrides. It offers detection limits in the range between ppb to ppt [92, 93]. Figure 7.3 shows the schematic diagram of the digestion unit coupled to HG/CV-AAS.

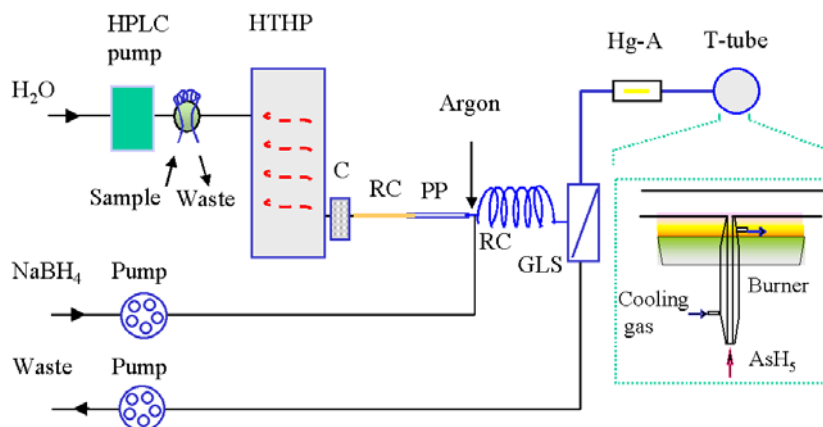


Figure 7.3 Schematic diagram of the digestion unit coupled with HG/CV-AAS. The insert is the T-shaped tube with cooling jacket. (HTHP: HTHP digestion unit, C: Cooler, RC: Restrictor capillary, PP: Polypropylene tube, RC: Reaction coil, GLS: Gas-liquid separator, Hg-A: Hg trapping unit (only for analysis of Hg))

A Perkin-Elmer AAS spectrometer (PE Flame 3030) was coupled to the high-temperature/high-pressure (HTHP) flow digestion system for quantitative determination of arsenic and mercury in biological and environmental samples.

A quartz T-shaped tube, shown in the insert of Fig. 7.3, was applied. The dimensions are 162 mm length (absorption path), 20 mm i.d. and 1 mm wall thickness. The inlet tube is 70 mm long and has 2 mm i.d. with a cooling jacket for Arsenic detection. An arsenic electrodeless discharge lamp (EDL) and a mercury hollow cathode lamp (HCL) were operated at currents of 8 mA and 12 mA, respectively. The analytical lines were As 193.7 nm and Hg 253.7 nm. A slit-width of 0.7 nm was used for both As and Hg detection. The signals from the analog output of the AAS-instrument were processed by a computer with HPLC software (Knauer, version 2.2).

Mercury was pre-concentrated as amalgam on gold wool placed inside a quartz tube. A piece of Ni-Cr wire (diameter 0.5 mm, resistance 1 Ω) was coiled around the quartz tube to heat the gold wool electrically. Mercury was trapped for a defined period on the gold wool at a temperature of 100 $^{\circ}\text{C}$, released by heating to 500 $^{\circ}\text{C}$, and finally transferred into the quartz tube by a defined Argon flow. The desorption of mercury was controlled by a temperature program.

Chapter 8

Investigation of the flow digestion system

8.1 Digestion conditions

The HTHP digestion system can be employed at high temperatures (up to 360 °C). Correspondingly, a high pressure should be maintained in order to avoid the formation of vapor. According to the saturated vapor-pressure diagram of water shown in Fig. 8.1 [94], a minimal back pressure of 144 atm (14.6 Mpa) is required to maintain exclusively a liquid phase if a temperature of 340 °C is desired for an aqueous digestion system.

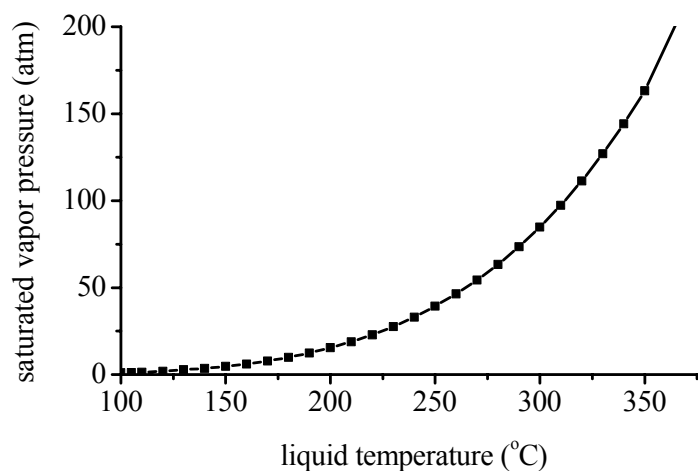


Figure 8.1 Saturation vapor-pressure diagram of water.

In order to obtain the back pressure within the digestion system, a section of PEEK capillary (i.d. 64 μm) is connected to the end of Pt/Ir capillary. A high back pressure is provided in the whole flow system by the HPLC pump working together with the restrictor capillary. In a laminar flow, the dimension of the restrictor capillary for a certain back pressure at a given flow rate can be calculated using the Hagen-Poiseuille law [95]

$$l = \frac{\pi \Delta p d^4}{128 v \eta} \quad , \quad 8.1$$

where l is the length of the capillary (m), d the capillary diameter (m), Δp the pressure drop (N/m^2), η the coefficient of viscosity (kg/ms) and v the flow rate of the liquid (m^3 per second). According to equation 8.1, a capillary of 35 cm length (64 μm i.d.) can build up a pressure of 170 bar at 1.2 mL/min flow rate. In experiment, a digestion temperature of 340 $^\circ\text{C}$ and a back pressure of 170 bar, higher than the vapor pressure of water at 340 $^\circ\text{C}$, were used.

Sample suspensions are delivered by carrier water through the whole system at a certain flow rate. High flow rate means less analysis time, which is limited by the minimum time of complete sample digestion and gas removal. For the digestion system, the heated Pt-Ir capillary length was 1 m. The sample reaction time can only be changed by the carrier flow rate. Generally, a relatively slow flow rate is advantageous for sample digestion, degassing and other processes. However, it is time consuming and results in wide signal profiles. Therefore, the carrier flow rates of 1.2 mL/min and 1.0 mL/min are chosen for HTHP-ICP-OES and HTHP-HG/CV-AAS, respectively.

The sample loop is nested in two split loops filled with acid. A sample is delivered through the first split loop before entering the heated Pt/Ir capillary. The length of the first split loop directly affects the sample diffusion and analysis time. Therefore, a 13 cm long tube (1.3 mm i.d.) was picked for the first split loop whereas a tube of 24 cm length with the same i.d. was selected for the second split loop.

Under these conditions, complete digestion of samples can be realized with nitric acid alone, which is sufficient in many cases. Fig. 8.2 compares the digested solution (clear, colorless) with the suspension of 2% Sewage Sludge (brown). The clear solution shows the effective digestion of a solid sample with the digestion system.

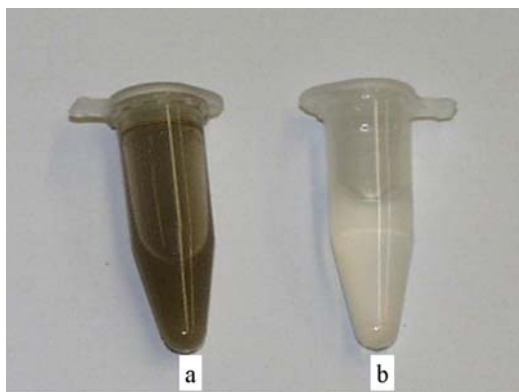


Figure 8.2 Comparison between a) 2% Sewage Sludge suspension and b) the digested solution.

8.2 Lifetime of the Pt/Ir capillary

Platinum dissolved from the Pt/Ir capillary surface for every single sample digestion procedure was determined using ICP-OES. The dissolved amount depends on the conditions inside the Pt/Ir capillary, such as the digestion temperature, acid concentration and sample matrix. Fig. 8.3 shows the effects of the digestion temperature and the nitric acid concentration. In each run about 0.49 μg Pt was dissolved from the inner surface with 2.5 M HNO_3 at a working temperature of 300 $^\circ\text{C}$. There is no significant influence of temperature in the range from 300 $^\circ\text{C}$ to 340 $^\circ\text{C}$, as can be seen in plot (b) of Fig. 8.3. The strong effect of acid concentrations on digestion is observed at a temperature of 320 $^\circ\text{C}$ as shown in plot (a) of Fig. 8.3. The signal of Pt could not be detected when only carrier water passed through the system, but more than 0.25 μg Pt per digestion was measured with 1 M nitric acid. The dissolved Pt amount increased by more than 140% when the nitric acid concentration was varied from 1 M to 7 M.

For the conditions commonly used (2.5 M nitric acid, 340 $^\circ\text{C}$, 1% suspension), 0.5 μg Pt was lost per digestion. Provided that the capillary is dissolved homogeneously and that up to a 5% loss of capillary material is acceptable for safety reasons, the capillary could theoretically stand approximately 500,000 digestions. However, it should be mentioned that a mixture of nitric and hydrochloric acids drastically reduces the tube lifetime. It was also found that hydrogen-peroxide enhances the dissolution of platinum, while the addition of hydrofluoric acid to the nitric acid had no effect on the amount of Pt dissolved.

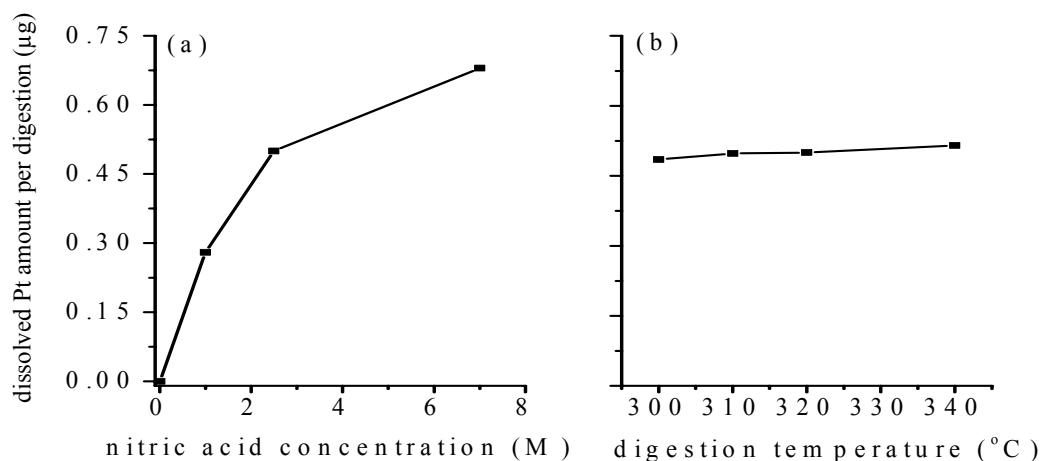


Figure 8.3 Dissolved Pt amount per digestion. (a) Effect of nitric acid concentration (320 °C) and (b) effect of working temperature (2.5 M HNO₃)

8.3 Element recovery

The recoveries of more than 30 elements were investigated at digestion temperatures from 100 °C up to 340 °C. A 10% ethanol solution replaced the standard reference material matrix as a “pure” organic matrix with added trace metals. Table 8.1 shows the recoveries of elements of interest. For most elements, the recoveries are better than 90% even at a digestion temperature of 340 °C. The losses of Fe and K occurred when the temperature was increased to 200°C. The significant losses of Ga, Ag and Sb occurred at temperatures above 100 °C (shown in Fig. 8.4). Much lower recoveries and worse precisions were acquired at a working temperature of 340 °C. For example, it was about 90 % for antimony at 340 °C.

Table 8.1 Recoveries (%) of elements at different digestion temperature

T (°C)	Ag	Al	As	B	Ba	Be	Bi	Ca
100	87	96	104	98	97	98	92	100
200	66	94	92	90	92	104	88	97
250	57	96	92	87	107	101	84	94
300	50	91	85	85	92	95	81	93
340	49±3	90±5	86±3	84±3	92±2	97±4	80±3	85±1
	Cd	Co	Cr	Cu	Fe	Ga	In	K
100	96	99	94	97	96	93	97	92
200	97	101	96	95	63	86	93	75
250	97	96	89	97	65	63	94	67
300	95	93	85	96	71	44	93	67
340	92±2	92±3	86±3	93±1	63±14	37±12	90±3	63±3
	Mg	Mn	Ni	Pb	Sb	Sr	Tl	Zn
100	100	100	97	96	85	96	99	100
200	98	97	98	99	27	98	94	100
250	96	97	96	97	19	94	97	91
300	95	93	91	90	15	95	98	93
340	95±2	92±2	91±3	90±4	12±2	95±2	91±3	90±2

Merck ICP standard and Perkin-Elmer ICP standard with traces of Sb added

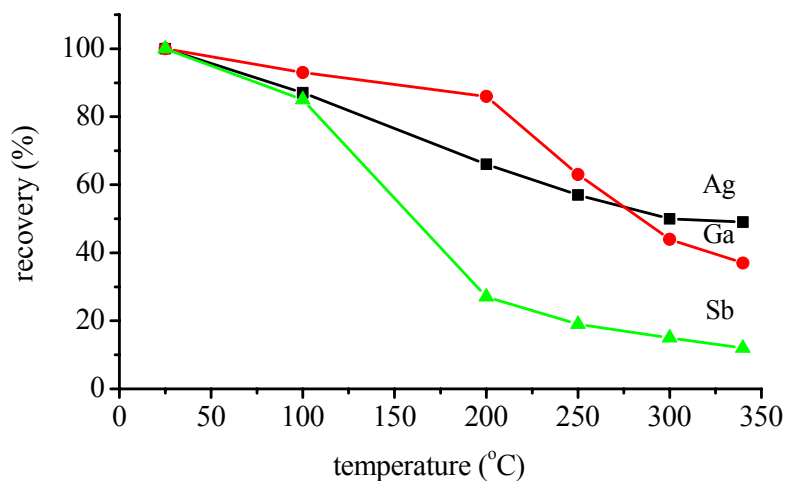


Figure 8.4 Recovery (%) of Ga, Ag and Sb vs. digestion temperature. (Organic matrix: 10 % ethanol; element concentration: 1 µg/mL Sb, 0.5 µg/mL Ag and Ga)

In order to investigate the reason for the element-based loss, another digestion system was made with a Tantalum capillary (2.0 mm o.d., 1.4 mm i.d., from Goodfellow GmbH) instead of Pt-Ir capillary. The recoveries of more than 30 elements have been measured

under the same conditions. Similar recoveries were obtained for all elements except Ag, although the recovery of Ag was significantly improved (more than 80% at 340 °C). The results of several elements are compared in Table 8.2. A mixture of nitric acid and hydrofluoric acid for sample digestion could result in considerably improved recoveries of these elements [82]. It is likely that the behavior, which was observed using pure solutions as well as digestion samples, is caused by the interaction of these elements with the tube material.

Table 8.2 Comparison of element recoveries using two digestion systems
(Pt-Ir capillary and Ta capillary)

T (°C)	Ag (%)		Fe (%)		Ga (%)		Sb (%)	
	Ta	Pt-Ir	Ta	Pt-Ir	Ta	Pt-Ir	Ta	Pt-Ir
100	99	87	101	96	102	93	87	85
200	99	66	94	63	97	86	41	27
250	94	57	85	65	83	63	27	19
300	88	50	58	71	43	44	13	15
340	83	49	33	63	29	37	10	12

8.4 Gas effects

8.4.1 The influence of reaction gas on the pressure in the system

Water as a carrier is delivered by a HPLC pump with a fixed flow rate in the whole system, which is run at a constant temperature. Without sample injection the pressure in the system is constant. However, the pressure rises quickly when a digestion reaction starts. The pressure change is caused by the formation of gaseous reaction products whose amount depends on the sample mass and the carbon concentration. The whole pressure in the system, as shown in equation 8.2, consists primarily of two parts: a constant pressure added by the HPLC pump working with a restricted capillary and the additional partial pressures of gaseous decomposition products (CO_2 , NO_x):

$$P_{total} = P_{constant} + P_{(\text{CO}_2+\text{NO}_x)}. \quad 8.2$$

Fig. 8.5 shows the relation between the gas formation rate and the system pressure for the digestion of a 1% Orchard Leaves suspension at 1.2 mL/min flow rate. The gas volume can be measured from a syringe coupled to the restrictor capillary and the corresponding pressure can be obtained from the read-out of the HPLC pump.

After a sample is delivered to the heated Pt/Ir capillary, sample digestion starts, resulting in gas formation and pressure increase. The system pressure rises from 14.7 MPa to 17 MPa with the gas-producing rate reaching 0.1 mL/s. The maximum pressure permitted for the quasi-closed digestion system is limited by the junction parts. In our experiment, 20% alcohol has been digested and 30 MPa pressure made no damage to the system. The interface length needed for efficient degassing during the short residence time depends on the maximum gas-formation rate. A gas removal interface will be discussed later.

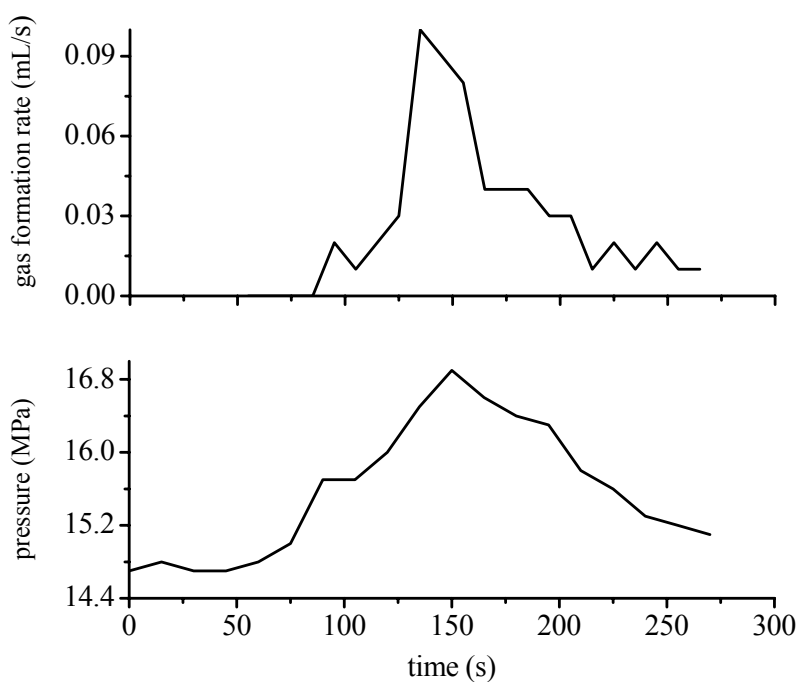


Figure 8.5 Relation between the gas formation rate and the system pressure. (Digestion of 1% Orchard Leaves suspension, 1.2 mL/min flow rate)

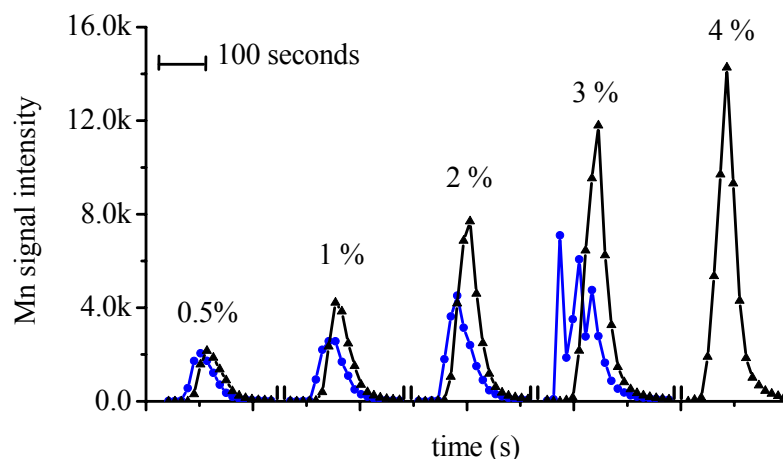


Figure 8.6 Determination of Mn in Tomato Leaves using various suspension concentrations, with (▲) and without (●) the gas removal interface.ⁱⁱⁱ Without polypropylene tube the signals of 3% suspension is strongly disturbed due to unstable plasma operation caused by the gases produced. No signal for 4% suspension could be detected without the polypropylene tube because the plasma was extinguished.

8.4.2 The influence of reaction gas on ICP-OES analysis

In order to investigate the effect of gaseous digestion products (CO_2 , NO_x) on the stability of the ICP, trace elements in a number of standard reference materials were determined. The sample loop volume was 0.6 mL and suspensions of the standard materials were used in concentrations between 0.5% and 4%. Fig. 8.6 shows the signals of the Mn 257.6 nm lines measured with the Tomato Leaves suspensions, with and without the gas removal interface. The data points represent intensities measured with 1 s integration time every 10 s. In the case of a suspension concentration of only 0.5 %, the amount of gases formed was relatively small and did not seriously interfere with the Mn determination. However, a suspension concentration of just 1% led to significant signal depression if the gases were not removed from the solution. Considering only the signals obtained without the degassing tube, Mn determination in a 2% suspension seems also to be possible, but the low signal to noise ratio caused by plasma instabilities led to a poor standard deviation (about 15%). In the case of a 3% suspension, the plasma was severely

ⁱⁱⁱ The data points are connected by full lines in order to guide the eyes.

disturbed and sometimes extinguished. The shape of the signal was not reproducible and, therefore, the data could not be used for quantitative measurements. No measurements could be carried out with 4% suspensions because the ICP was extinguished. On the other hand, suspensions of this concentration could be digested online without any influence on the plasma when the porous tube was used as an interface between the digestion system and the ICP spectrometry instrument. Very large and sharp signals were obtained for all suspensions, as can be seen in Fig. 8.6. Very similar results were obtained for all other elements and matrices.

8.4.3 The influence of reaction gas on HG/CV-AAS analysis

In contrast to the flame AAS, a direct coupling of the digestion system to a hydride/cold vapor generation-AAS system was unsuccessful. Firstly, NO_x as a strong oxide consumes lots of reductant and affects the formation of hydride/cold vapor. Secondly, NO_x has a strong molecular absorbance below 200 nm, which produces spectrum interference for the measurement of arsenic. Furthermore, the sudden degassing of a solution at the outlet of the restrictor capillary results in a strongly pulsed flow, which caused problems in controlling the chemical reaction in the hydride (cold vapor) generation system.

The influence of reaction gas was investigated by the analysis of arsenic in a series of samples prepared from 2% Orchard leaves suspensions with added arsenic standards. Thus, the suspensions contained the same matrix but with arsenic concentrations from 0.2 mg/mL to 0.6 mg/mL. Each sample was measured with and without the gas removal interface. The same amount of gases was formed during the digestion in all measurements. The obtained arsenic absorption signals are compared in Fig. 8.7. The arsenic signal increased with increasing concentration with degassing the solution, whereas, there was no linear dependence of the signal on concentration without degassing, and strong NO_x signals with similar peak height were recorded.

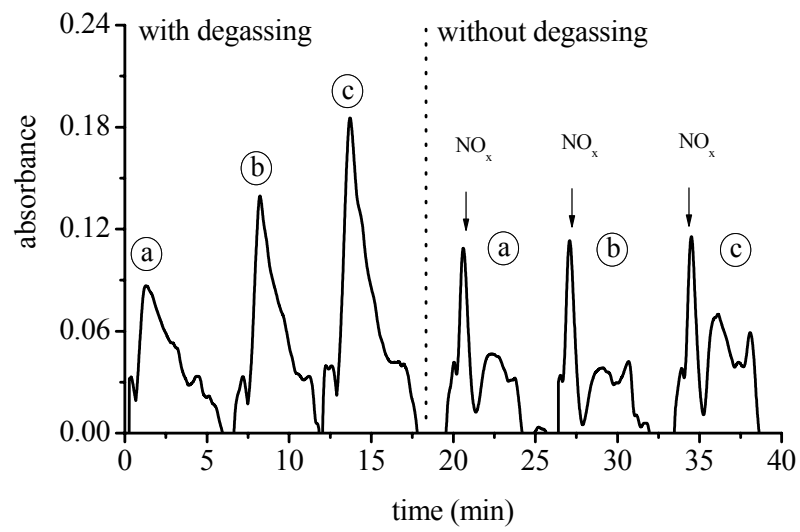


Figure 8.7 Comparison of arsenic signals obtained from a series of suspensions with the same matrix of 2% Orchard leaves, with and without the gas removal interface. (Arsenic concentrations are (a) 0.2 mg/mL, (b) 0.4 mg/mL and (c) 0.6 mg/mL)

Chapter 9

Investigations of gas removal

9.1 Optimization of the gas removal interface

The simplest arrangement for online element determinations is the direct connection of the outlet of the digestion system to the sample introduction unit (such as a nebulizer) of a detection instrument. As discussed in Chapter 8, this simple coupling cannot be used in the case of ICP spectrometry and HG/CV-AAS. Therefore, the outlet of the digestion system was connected with the nebulizer of an ICP-OES instrument or with the hydride (cold vapor) generation system via various permeable tubes, such as silicon, ceramic and polypropylene tubes (Table 9.1).

There was only a very small pressure drop in the tube ($< 1\text{kPa}$) using such connections because of the relatively small flow rate which was limited by the time of the flow digestion process and caused by the relatively large inner diameter of the porous tube. In order to enhance gas exchange through the tube wall, the pressure inside the tube was increased by attaching a short piece of PEEK capillary with a small inner diameter in front of the porous tube. The degassing tube was now fitted between two restrictor capillaries, as shown in Fig. 9.1(a). The first capillary ($64\ \mu\text{m}$ i.d.) with a very high pressure drop delivered the necessary back pressure for the sample digestion unit. A

PEEK capillary with 130 μm i.d. and an appropriate length was chosen for the second one to obtain a pressure drop of 10 kPa up to some hundreds of kPa.

Table 9.1 Various tubes used for gas removal interface

Type	Dimension	Supplier
Silicon tube	i.d.: 0.2 – 0.5 mm, o.d.: 0.3 – 1.0 mm, wall thickness: 0.1 mm, 0.2 mm and 0.25 mm, length up to 1 m	Reichelt, Karlsruhe, Germany
Ceramic tube	i.d.: 0.5 – 2.6 mm, o.d.: 3 mm, length: 100 mm, pore size: 1 μm	Hermsdorfer Institut für Technische Keramik, Hermsdorf, Germany
Porous polypropylene tube	a) i.d.: 1.8 mm, o.d.: 2.7 mm, pore size: 0.2 μm and 0.1 μm , bubble point: 0.32 and 0.4 MPa b) i.d.: 0.6 mm, o.d.: 1 mm, pore size: 0.2 μm , bubble point: 0.32 MPa, length: up to 1 m	Microdyne, Wuppertal, Germany

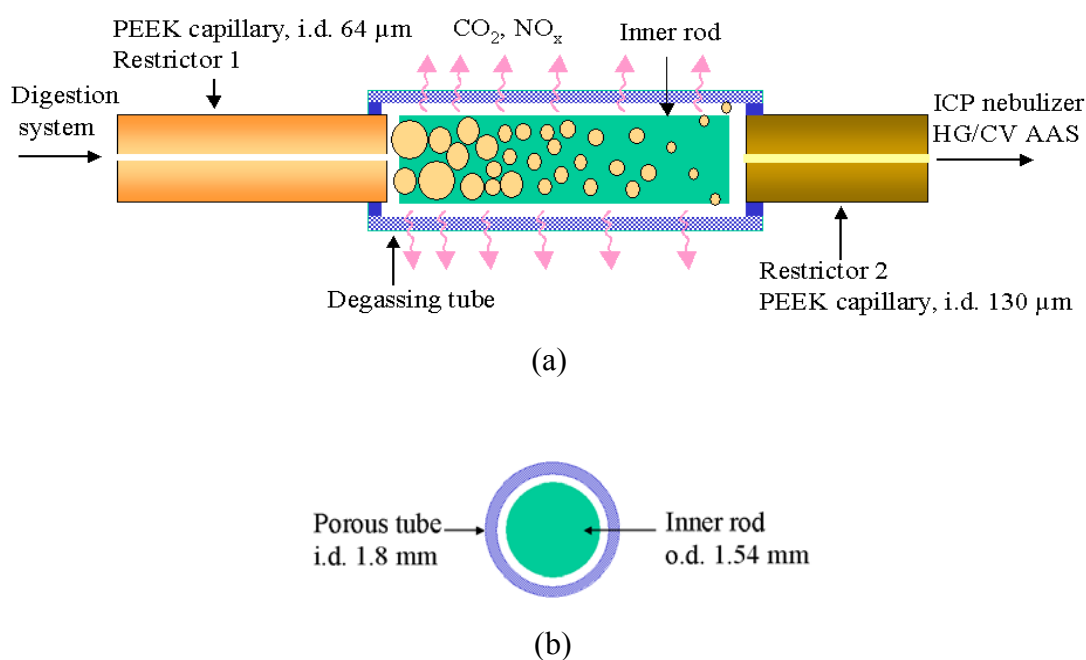


Figure 9.1 Schematic diagram of the gas removal interface. (a) Arrangement of the gas removal interface and (b) cross section of the porous tube with an inner rod.

9.1.1 Silicon/Ceramic tube

Investigations with various tube materials showed that, in the case of thin-walled silicon (0.1 mm), a tube length of some meters would be necessary for effective degassing since the permeation rate of this non-porous material is low. Furthermore, it was observed that the silicone tubing was destroyed at internal pressures > 50 kPa.

The mechanical properties of ceramic tubes are ideal for the use at high pressures, but a low bubble point results from the relatively large pore size (> 1 μm) and the hydrophilic properties of such tubes. Therefore, liquid was also forced through the porous walls even with very small pressure. The bubble point could be increased considerably by silylation of the ceramic tube with dimethyldichlorosilane [96], but the hydrophobic surface obtained by silylation was destroyed by the strongly oxidizing solution after a few digestion procedures. Another disadvantage of this material is the difficulty to handle the extremely fragile thin-walled capillaries.

9.1.2 Polypropylene tube

Three different sized polypropylene tubes (described in Table 9.1) have been investigated as gas removal interfaces. The use of a tube with dimensions of 1.8 mm i.d., 2.7 mm o.d., and 0.1 μm pore size did not improve the gas separation. The dead volume of a 30 cm long tube (760 μL) is similar to the volume of the injected sample (600 μL), which unavoidably leads to dilution of the sample by dispersion. A polypropylene tube with 0.2 μm pore size but only 0.6 mm i.d. and 1 mm o.d., and thus with a smaller dead volume, was tested for comparison. However, no improvement in gas removal was found. The explanation for this behavior might be that, on the one hand, the diffusion of gases is better because of the smaller inner diameter and the thinner walls. On the other hand, the diffusion of gases is reduced because of the smaller surface area and the shorter residence time of the sample at a given flow rate.

The best degassing results were obtained with a polypropylene tube (2.7 mm o.d. and 1.8 mm i.d.) having a pore size of 0.2 μm . The maximum back pressure for this tube is given by the bubble point of the material (320 kPa), but pressures close to the bubble point affect its lifetime.

The gas removal performance of a porous tube can be shown by the ratio of the outlet-dissolved-gas concentration (c_o) to the inlet-dissolved-gas concentration (c_i), which is illustrated by [97]

$$\frac{c_o}{c_i} = e^{-kal/v} \quad , \quad 9.1$$

where a is the surface area of a tube (m^2), l the length of a tube (m), v the velocity of the liquid (g/s), and k the mass-transfer coefficient (g/m^3s), which describes how quickly gas can pass through the liquid medium, the membrane and the gas in the pores. The total transfer coefficient (k) depends on the individual transfer coefficients (k_l, k_m, k_v) [97]

$$\frac{1}{k} = \frac{1}{k_l} + \frac{1}{k_m} + \frac{1}{k_v} \quad , \quad 9.2$$

where k_l, k_m and k_v represent transfer coefficients through the liquid phase, the membrane and the vapor phase, respectively. The resistance ($1/k$) to the transport can be described as the reciprocal of the total transfer coefficient (k). Yang and Cussler [98] have experimentally verified that the dominant resistance is in the liquid phase, the resistance in the gas phase and the membrane is much smaller. Therefore, reducing the diffusion distance in the liquid phase can significantly decrease the resistance, resulting in high gas removal efficiency.

A 1/16'' (1.58 mm) PEEK capillary with closed ends was inserted into the porous tube of 1.8 mm i.d., serving as an "inner rod", as shown in Fig. 9.1 (b). The profile of the liquid passing through the porous tube can be considered as a ring with a thickness of only 0.1 mm if the inner rod is ideally centered. Thus, the liquid has the properties of a film on the inner surface of a porous tube. The dead volume in this arrangement is only 175 μ L for a 30 cm long tube (without inner rod it is 760 μ L). Very efficient degassing was achieved due to the significantly improved ratio of surface area to volume, and the short diffusion distance to the walls. After the digested solution had passed not more than 15 cm of this rod filled tube, the efficiency of gas removal was 98% (see Fig. 9.2). This is better than with a 35 cm porous tube of 0.6 mm i.d. and 1 mm o.d.. Using a tube of 20 cm length, no gases were collected in a gas tight syringe.

The porous polypropylene tube with the "inner rod" resulted in the best performance for effective gas removal from the digested solution. It was used for all further

investigations as the interface between the sample digestion unit and the detection instruments. Keeping the standard working conditions of a sample flow rate of 1.2 mL/min and a back pressure of about 270 kPa (real pressure inside the tube is less than 270 kPa because of the holes), one tube can be used for more than 6 months.

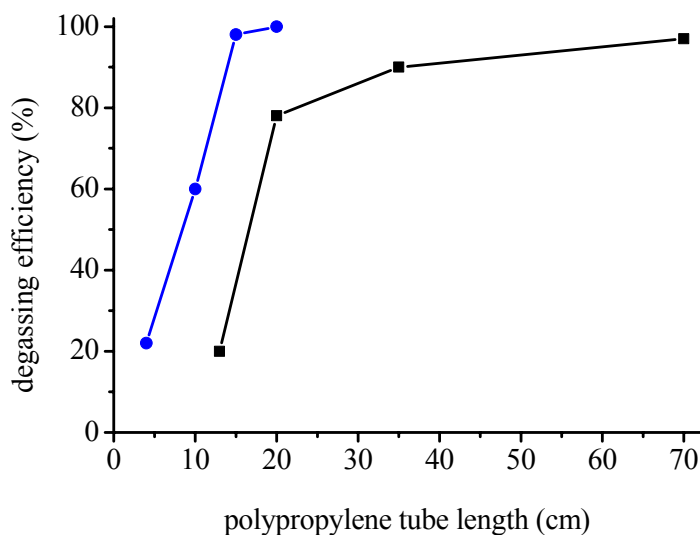


Figure 9.2 Comparison of degassing efficiency between two polypropylene tubes with 0.2 μm porous. (-■- i.d./o.d.: 0.6/1.0 mm and -●- i.d./o.d.: 1.8/2.7 mm, with an “inner rod” of 1.58 mm o.d.)

9.2. Gas removal efficiency

The efficiency of the gas removal using the polypropylene tube was determined in three ways. (i) The total volume of gases (NO_x , CO_2) was collected using a syringe, (ii) the residual NO_2 was measured by AAS, and (iii) the residual carbon was determined by ICP-OES.

First, the total volume of the gaseous reaction products and the gas formation rate during the digestion procedure were measured by coupling a gas tight syringe to the restrictor capillary in front of the polypropylene tube. The total gas volume was read out in this way and the gas formation rate can be calculated. However, accurate results of residual gases could not be given by this method.

The second method was realized by the measurement of the molecular band absorption of NO_2 . Here, the solution was delivered into a small gas/liquid separator

vessel, where the gases (CO_2 , NO_x) were transported in an argon carrier stream (200 mL/min) into an absorption cell, i.e. a 10 cm quartz tube positioned in the optical path of an AAS-instrument. NO_2 was measured by absorption at 238 nm using the prominent Ag emission line from an Ag hollow cathode lamp. Fig. 9.3 shows the NO_2 absorbance using porous polypropylene tubes of 10 cm and 30 cm length (2.7 mm o.d., 1.8 mm i.d and 0.2 μm pore size), and the corresponding signals when there was no prior gas removal. The sample was a 1% Tomato Leaves suspension and the sample volume 0.6 mL. Using a 10 cm long tube nearly 70 % of reaction gases passed through the wall of the tube interface, while more than 95 % gases could be removed with a tube of 30 cm length.

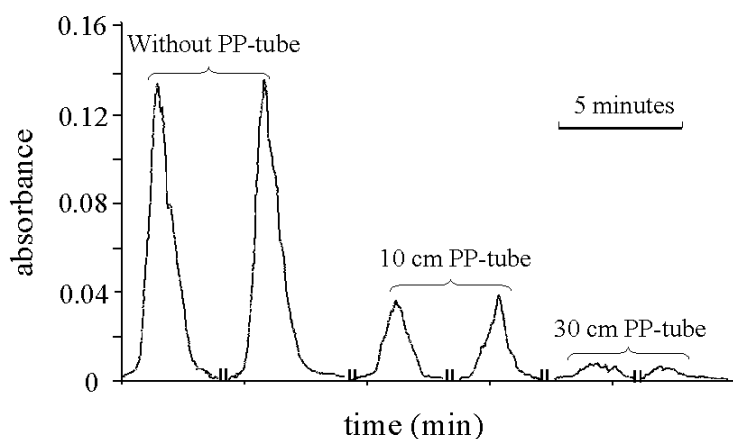


Figure 9.3 Absorbance of NO_2 molecular bands at 238 nm as an indicator of gas removal efficiency using polypropylene (PP) tubes of 10 and 30 cm length, respectively. (Without an inner rod)

Finally, the carbon emission lines (the strong line at 193.1 nm and the weak line at 247.8 nm) can be used as an indicator of carbon dioxide which has passed through the nebulizer and introduced into the ICP. At a working temperature of 340 °C, it can be expected that all carbon in the suspension is oxidized to carbon dioxide. Within the high-pressure flow system (more than 17 MPa) this carbon dioxide is totally dissolved in the liquid phase, but degassing of the sample solution could occur after pressure release behind the restrictor capillary of the digestion system. However, still a small amount of carbon dioxide is dissolved in the solution.

Carbon signals (247.8 nm) for digestion solutions of 1% Tomato Leaves suspensions with and without gas removal are shown in Figure 9.4. The digestion solution can be effectively degassed using a 20 cm polypropylene tube with an inner rod. Unfortunately, a

determination of carbon at this low concentration was impossible using the weak C 247.8 nm line. The signal intensity was in the range of the background noise.

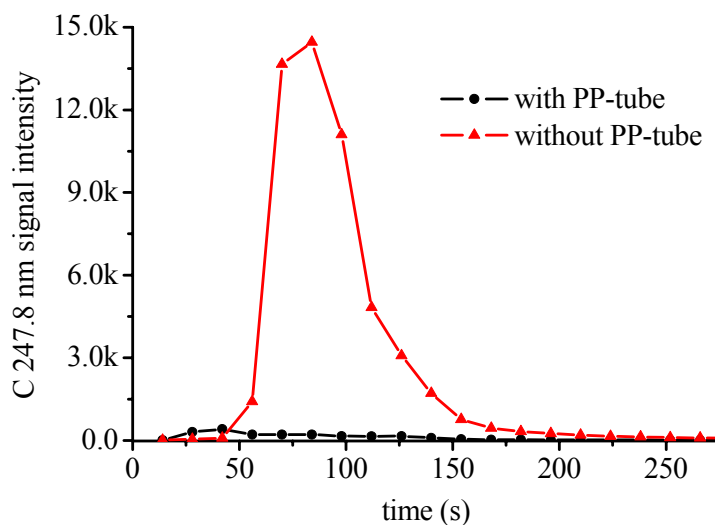


Figure 9.4 Signal profiles of C 247.8 nm for digestion solutions of 1% suspensions of Tomato Leaves, with (-●-) and without (-▲-) the gas removal interface (20 cm polypropylene (PP) tube with an inner rod).

However, using the carbon line at 193.1 nm the low C concentration could be measured. The digestion solutions of 0.5% to 4% suspensions were measured under the same conditions. The plasma was observed to be stable even with the 4% suspensions. Double peaks were obtained for higher concentrations, as shown in Fig. 9.5. A possible reason for the double peaks is that the residual gaseous carbon dioxide reaches the plasma earlier than the dissolved carbon dioxide. The peaks caused by the gaseous carbon dioxide increase with suspension concentration, but the peaks resulted from dissolved carbon dioxide had similar strengths. It can be seen in Fig. 9.5 that the signals slightly increase when the suspension concentration is changed from 0.5% to 4%. However, the “residue carbon” is estimated to be not higher than 0.5% even for the digestion of a 4% suspension. It should be noted that this value represents the sum of the undigested carbon (the true residual carbon), the unmoved gaseous carbon dioxide and the dissolved carbon dioxide. This low “sum-value” indicates that the flow digestion system operated at 340 °C provides complete digestion of solid samples and the polypropylene tube can efficiently

degas the solution. In all experiments, carbon signals were simultaneously measured as an indicator for all matrices und suspension concentrations under investigation.

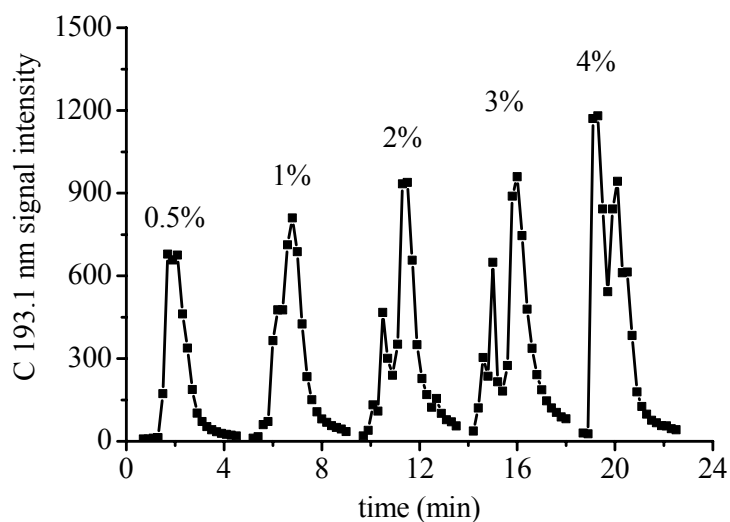


Figure 9.5 Signals of C 193.1 nm from digestion solutions of 0.5 %, 1%, 2%, 3% and 4% Tomato Leaves suspensions.

Chapter 10

Online coupling of the flow digestion system with ICP-OES

This chapter describes the experiments for evaluating the potential and limitations of the high-temperature/high-pressure flow digestion system coupled with an ICP-OES instrument. The accuracy and reliability of the entire online procedure are demonstrated by element analysis of various standard reference materials.

10.1 Experimental

Deionized water obtained from a Milli-QTM water purification system was used as carrier and for the preparation of solutions. Nitric acid (65%, analytical grade, Merck, Darmstadt, Germany) was purified with a sub-boiling distillation apparatus made of quartz and heated by infrared radiation (Hereaus Quarzschmelze, Hanau, Germany). Standards were prepared for the element measurements by stepwise dilution of ICP multi-element standard solutions containing 1000 mg/L for each element (Merck, Germany, Perkin Elmer, USA). In order to verify the efficiency and reliability of the coupling between the digestion system and the ICP-OES instrument via a porous tube, various

standard reference materials (Table 10.2) were used. Samples were prepared in 2.5 M HNO₃, which was sufficient to digest all samples up to 4% suspensions.

The main steps for sample analysis include sample introduction, digestion, gas removal and elemental determination. The sample suspension and the nitric acid are introduced to the flow digestion system by two valves. The suspension is nested between two acid plugs, as shown in Fig. 10.1, which prevent dispersion of the sample into the carrier water. It is then transported through the heated Pt/Ir capillary with a residence time of about 40 s at a flow rate of 1.2 mL/min, producing the digested solution. Before degassing the solution, the mixture of gas and liquid is cooled down via an air cooler. Finally, the gas-free solution is analyzed using the ICP-OES spectrometer.

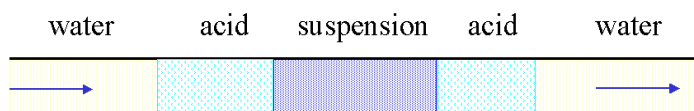


Figure 10.1 Flow diagram of embedded suspension injected by two valves.

10.2 Connection between polypropylene tube and the nebulizer

Meinhard nebulizers are widely used for nebulization of solution in ICP spectrometry. This kind of nebulizer with a small venturi end creates a pressure gradient across the sample capillary by a high-velocity gas stream, which causes a natural solution uptake [1]. The vacuum pressure, which is proportional to a gas flow rate, can be calculated according to Hagen-Poiseuille law (see equation 8.1). In routine analysis, a peristaltic pump is used to control the solution introduction to a nebulizer. However, the flow rate is restricted by a HPLC pump when the flow digestion system is coupled with the ICP-OES instrument. The application of an additional peristaltic pump is unnecessary. The vacuum pressure caused by a nebulizer significantly lowers the gas removal efficiency of a polypropylene tube.

A capillary was connected to the inlet of the nebulizer to minimize this effect. A 5 cm long capillary (130 μm i.d.) worked well for the optimized nebulizer gas flow rate of 0.5 mL/min. Thus, the capillary between the gas removal interface and the nebulizer, i.e. the

second restrictor shown in Fig. 9.1(a), was 12 cm, which applied the same pressure to the polypropylene tube as when using a 7 cm long capillary without coupling to the nebulizer.

10.3 Signal collecting mode

A sample transported in a carrier stream (water) to the ICP instrument results in the transient signal typical for flow injection systems. A time-resolved mode is available in the ICP-OES instrument used. However, in this mode the measurements of element emission lines are done either in a low or in a high wavelength range and not all chosen element lines are covered in a single run. Therefore, the standard software was modified to increase the number of measurements for one sample injected from 10 (standard) to 20 or more. It was found that 20 measurements were sufficient to cover the whole peak area as well as the background before and after the peak. Fig. 10.2 shows the Mn signals from the 260.5 nm line for 7 repetitive measurements of a 1% Spinach suspension. RSD of the signal areas was less than 2%. 20 consecutive measurements were made for simultaneous analysis of all elements of interest. The total analysis time was 240 seconds under the usual operating conditions, i.e. 0.6 mL sample volume and 1.2 mL/min flow rate.

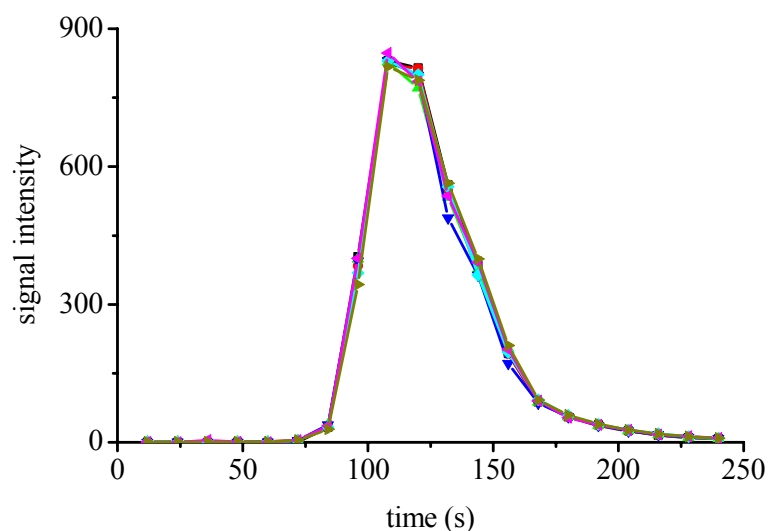


Figure 10.2 Mn 260.5 nm signals of seven repetitive measurements of 1% Spinach suspension.

10.4 Sample determination

Several biological and environmental standard reference materials have been studied using the flow digestion system coupled with the ICP-OES and using the conditions listed in Table 10.1. The standard addition method was used for element determinations. Linear calibration curves with correlation coefficients of better than 0.995 were received in all cases.

Table 10.1 Instrumental and analytical parameters for the flow digestion system coupled with ICP-OES

Digestion conditions		
Temperature	340 °C	
Pressure	>170 bar	
Flow rate	1.2 mL/min	
ICP conditions		
Rf generator power (W)	1350	
Auxiliary gas (L/min)	0.5	
Nebulizer gas (L/min)	0.5	
Nebulizer type	Meinhard	
Spray chamber	Cyclone type	
Integration time (s)	High wavelength range: 1s	
	Low wavelength range: 1s	
Analysis wavelength (nm)		
Al 396.15, 257.51	Cr 267.71	Mo 204.59
B 249.77	Cu 324.75	Ni 231.60
Ba 233.52	Fe 259.94	Pb 220.35
Ca 396.84	Mg 279.07, 279.55	Sr 407.77
Cd 226.50	Mn 259.27, 257.6	Zn 202.54

The comparison of measured and certified values including standard deviation (N=4) is shown in Table 10.2. The element concentrations in the samples were determined from 0.5% to 2% sample suspensions in 2.5 M nitric acid. As seen in Table 10.2, there is good or acceptable agreement between certified and measured values for most elements, while relative standard deviations based on four measurements were low. As an exception, the determination of iron in two matrices resulted in a discrepancy between certified and measured values. As discussed in Chapter 8, Fe has a loss of 30% to 40% at high temperature due to the interaction of Fe and the Pt-Ir material.

Table 10.2 Determination results of trace elements in certified standard materials (mg/kg)

Elements	Bovine Liver NBS 1577a		Tomato Leaves NBS 1573		Orchard Leaves NBS 1571		Pine Needles NBS 1575		Spinach NBS 1570		Bovine Liver CRM185	
	CV	MV	CV	MV	CV	MV	CV	MV	CV	MV	CV	MV
Al							545±30	567±23	870±50	817±30		
B			30	28±2	33±3	32±6			30	27±1		
Ba					44	41±2						
Ca											131	133±3
Cr			4.5±0.5	5.0±0.8	2.6±0.3	2.3±0.4	2.6±0.2	2.9±0.5	4.6±0.3	4.0±0.8		
Cd			3.0 (nc)	3.1±0.4								
Cu	158±7	149±1	11±1	10.9±1.3	12±1	11.9±0.9	3.0±0.3	3.1±0.3	12±2	13.0±0.7	189±4	184±7.0
Fe	194±20	194±36	690±25	681±30	300±20	258±40	200±10	262±40	550±20	492±32	214±5	199±21
Mg	600±15	615±14									634	663±18
Mn	9.9±0.8	9.3±0.3	238±7	231±13	91±4	87±2	675±15	690±10	165±6	166±3	9.3±0.3	9.2±0.2
Mo	3.5±0.5	3.1±0.5										
Ni									6	6.5±0.4		
Pb			6.3±0.3	6.5±0.6			10.8±0.5	9.7±1.5				
Sr			44.9±0.3	44.7±2.3	37±1	33±1	4.8±0.2	4.6±0.1	87±2	93±1		
Zn	123±8	124±2	62±6	61±6	25±3	23±2			50±2	49±1	142±3	127±5

CV: Certified value, MV: Measured value, nc: non-certified value

The detection limits (3SD: standard deviation of the noise, N = 10) were determined using blank samples containing only 2.5 M nitric acid under identical conditions as for the sample analysis. The measurements lead to detection limits related to the element concentration in the solution, which are then calculated for the element content in 1% suspension samples, as shown in Table 10.3. The detection limits are about 1 µg/g or lower for all elements, except Fe and Pb. For Pb the low ICP-OES detection sensitivity is responsible for the high detection limit. In the case of Fe, a relatively strong blank value led to the high detection limit. The signals from 9 consecutive measurements of Mn in 1% Spinach suspension are shown in Fig. 10.3. The relative standard deviation (RSD) was 2.3%.

Table 10.3 Detection limits (DL) for selected elements in a 1% suspension (N= 10)

Element	Wavelength (nm)	DL (µg/g)	Element	Wavelength (nm)	DL (µg/g)
Al	257.51	0.30	Mn	257.6	0.40
B	249.77	0.52	Mg	279.07	0.70
Ba	233.52	0.44	Mo	206.6	0.50
Ca	396.84	0.60	Ni	221.6	0.60
Cd	226.5	0.73	Pb	220.35	2.6
Cr	267.71	0.89	Sr	407.77	0.20
Cu	324.75	0.44	Zn	202.54	0.64
Fe	259.94	3.0			

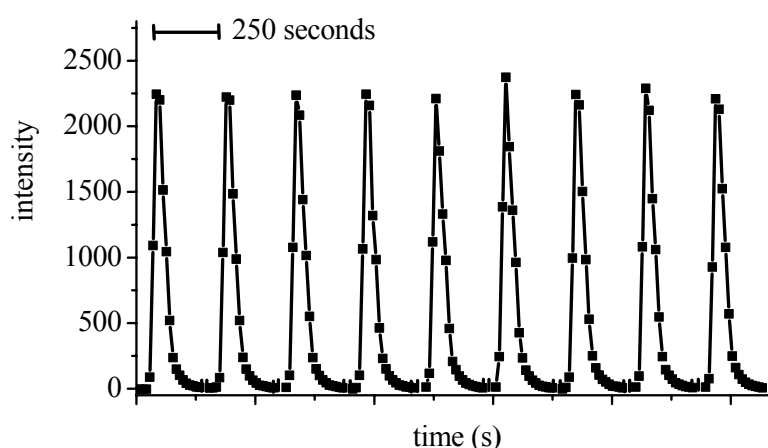


Figure 10.3 Signals obtained from 9 consecutive measurements of Mn in 1% Spinach suspension, RSD: 2.3%. (The data points are connected by full lines in order to guide the eyes).

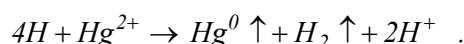
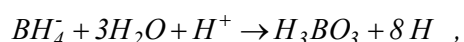
10.5 Sampling frequency

The total dead volume of the digestion system including the nested sample loop, the first split loop, the Pt/Ir capillary and the gas removal interface is 2.2 mL. With a standard flow rate of 1.2 mL/min, the shortest time for sample digestion and gas removal was about 200 s due to the sample dispersion. Considering the time required for the ICP measurement procedure, the total time for sample analysis was between 250 and 300 s. However, the advantage of flow systems is that the next sample can be introduced before the previous sample has left the system, resulting in a higher sample throughput. A throughput between 12 and 15 samples/h can be achieved depending on the sample and the suspension concentration.

Chapter 11

Online coupling of the flow digestion system with HG/CV-AAS

This chapter will report on the coupling of the high-temperature/high-pressure flow digestion system with the HG/CV-AAS instrument for online arsenic and mercury analysis. The gas-free solution was transported through a hydride generation coil, where volatile species were formed. The mechanisms for the generation of volatile As compound and of Hg vapor can be described as



The generated vapor was then carried by an Ar stream into a T-shaped quartz tube for detection. The amalgam technique was applied in analysis of mercury. The reliability of the HTHP-HG/CV-AAS method was tested by analyzing arsenic and mercury in several reference materials. The signal area was integrated instead of measuring the peak heights.

11.1 Optimization of operation conditions

340 °C working temperature, more than 170 bar back pressure and a flow rate of 1.0 mL/min were used in the sample digestion system. Other operation conditions were

investigated with univariant optimization of sensitivity and peak shape. The optimum values of these operating parameters are summarized in Table 11.1. Several parameters having significant effects on elemental analysis are discussed below.

Table 11.1 Instrumental and analytical parameters for HG/CV-AAS

Atomic absorption spectrometer	
Arsenic	
Wavelength	193.7 nm
Lamp current (EDL)*	8 mA
Slit	0.7 nm
Read time	0.1 s
Acetylene flow rate	26 mL/min
Air flow rate	67 mL/min
Cooling gas flow rate (for inlet arm of T-shaped tube)	3.3 L/min
Mercury	
Wavelength	253.7 nm
Lamp current (HCL)*	12 mA
Slit	0.7 nm
Read time	0.1 s
Hydride/Cold vapor generation	
NaBH ₄ solution concentration	0.5% (0.01 M NaOH)
NaBH ₄ flow rate	1.2 mL/min
Carrier gas flow	2.5 L/h (Ar)
GLS* volume	3.5 mL
Trapping unit for Hg	
Trapping medium and size	Gold wool, 1 cm length
Resistance wire	Ni-Cr, 1 Ω
Heating temperature and time	100 °C 4 min, 500 °C 20 s

* EDL: Electrodeless discharge lamp

HCL: Hollow cathode lamp

GLS: Glass-liquid separator

11.1.1 Optimization of the carrier gas flow rate

Argon was used to separate hydride and mercury from the liquid applying a gas-liquid separator. The effects of the argon flow rate on the arsenic and mercury detection sensitivities were investigated with flow rates between 1.0 L/h and 4 L/h. As shown in Fig. 11.1, the signal intensities of As and Hg are very low at 1.0 L/h due to the low transport efficiency. Both signals increase with the increasing flow rates. However, the

effects on As and Hg signals were different for flow rates > 2.5 L/h because a trapping unit (see Fig. 7.3) was additionally used for Hg analysis. Therefore, a flow rate of 2.5 L/h was chosen for analyses of As and Hg.

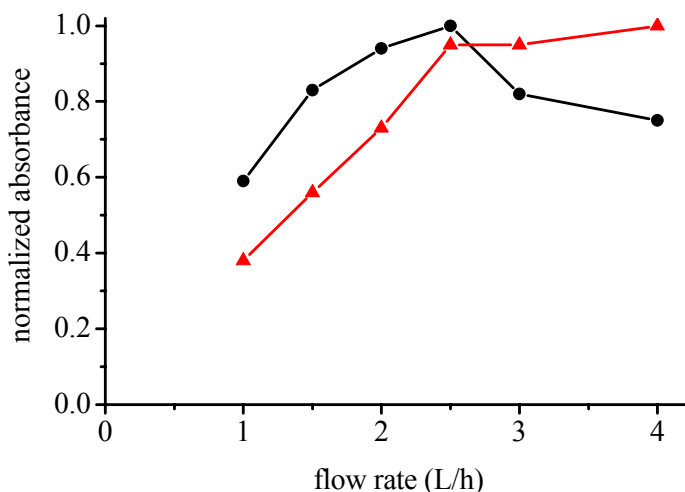


Figure 11.1 Influence of the carrier gas flow rate on (-▲-) arsenic and (-●-) mercury analyses.

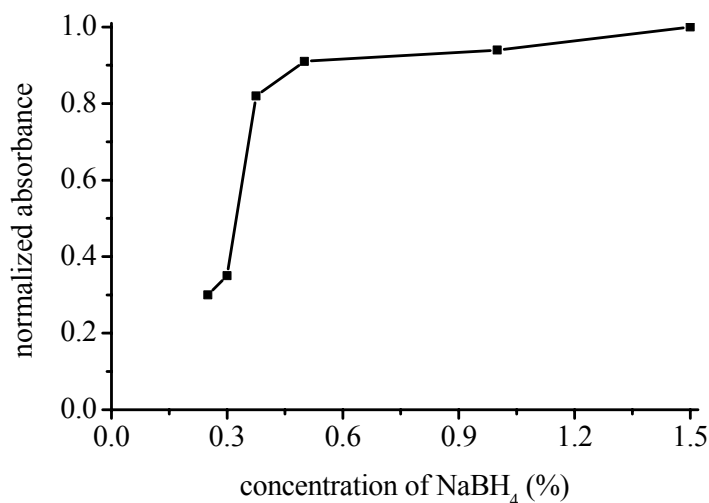


Figure 11.2 Optimization of NaBH₄ concentration (% w/v) at a flow rate of 1.2 mL/min.

11.1.2 Optimization of the NaBH₄ concentration

The concentration of sodium borohydride (NaBH₄) was optimized at a fixed flow rate of 1.2 mL/min. Fig. 11.2 shows the concentration effects on arsenic signals in the analysis of 1% Orchard Leaves suspensions. The signals were significantly depressed at

concentrations lower than 0.38%, while strong signals were obtained at concentrations of above 0.5%. For NaBH₄ concentrations higher than 1%, some foam was formed in the gas-liquid separator, resulting in an inferior performance. Similar effects due to NaBH₄ were also observed in Hg analysis. Therefore, 0.5% NaBH₄ and a flow rate of 1.2 mL/min were used for all further analyses.

11.1.3 The effect of cooling the inlet arm of the T-shaped quartz tube

Hydride was carried by inert gas into a T-shaped tube mounted in the flame for atomic absorption measurement. The temperature in the inlet arm of the T-shaped tube was significantly high to decompose a part of the hydride. A T-shaped tube with a cooling jacket, shown in the insert of Fig. 7.3, was made for As measuring. Early decomposition of hydride was avoided by air cooling with flow rates higher than 3 L/min. 50 µg/mL, 25 µg/mL and 10 µg/mL arsenic in Orchard Leaves suspensions have been determined with and without cooling the inlet arm. As shown in Fig. 11.3, low background and strong signals are obtained with cooling the inlet arm.

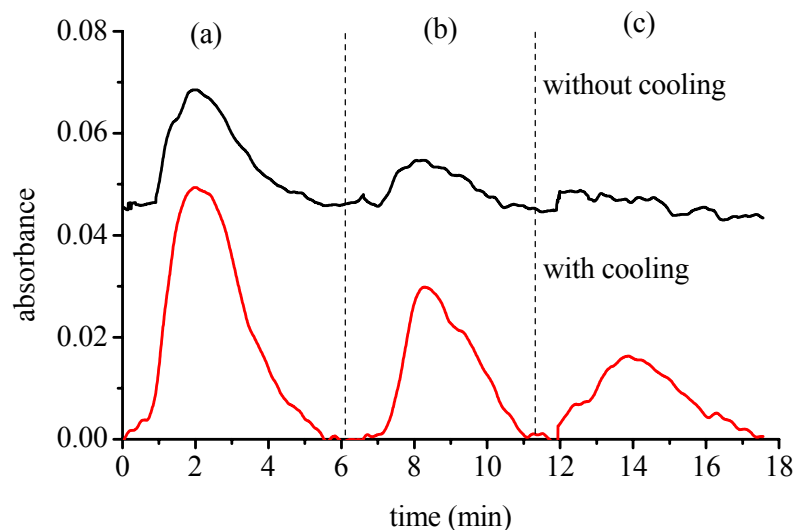


Figure 11.3 Comparison of arsenic transient signals of (a) 50 µg/mL, (b) 25 µg/mL and (c) 10 µg/mL arsenic in Orchard leaves suspensions with and without cooling the inlet arm of the quartz T-shaped tube.

11.2 Arsenic analysis

In order to verify the applicability of the HTHP flow digestion system coupled with the HG-AAS via the polypropylene tube, arsenic in five reference materials was analyzed. The arsenic standard solutions were prepared from As (V) stock solution of 1.000 g/100 mL in 0.5 M HNO₃ (Titrisol[®] Merck Art. 9939). The reductant solution was prepared by dissolving appropriate amounts of powdered sodium borohydride (E. Merck, Germany) and stabilized with sodium hydroxide (Merck, Germany) of 0.01 M concentration.

The experimental arsenic data agree fairly well with the certified values for the investigated reference materials as shown in Table 11.2. The only exception was Sea Lettuce, where a lower value was measured. Sea Lettuce was not completely digested using only nitric acid because of some SiO₂ content.

The reproducibility of repetitive measurements was assessed by analyzing 1% Rice Flour suspension. Ten consecutively measured As signals are shown in Fig. 11.4. The RSD of the measurements was 4%. A detection limit (3SD) of 0.07 µg/g was found for As.

Table 11.2. Certified and experimental concentrations of arsenic
in reference materials (µg/g)

Reference material	Certified value	Measured value
NBS 1568 Rice Flour	0.29	0.31±0.04
NBS 1571 Orchard Leaves	10±2	10.6±0.6
BCR 279 Sea Lettuce	3.09±0.2	2.5±0.2
NBS 1573 Tomato Leaves	0.27±0.05	0.27±0.04
NBS 1570 Spinach	0.15±0.05	0.13±0.05

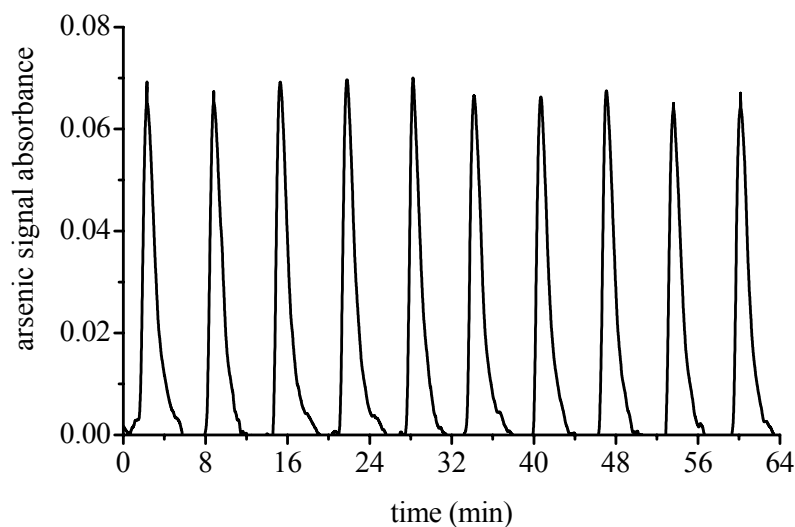


Figure 11.4 Ten consecutively measured arsenic signals obtained with 1% Rice Flour suspension.

11.3 Mercury analysis

The Hg vapor, generated in a cold vapor (CV) generation system, was pre-concentrated by trapping on the gold wool as amalgam. Subsequently it was released by heating the gold wool to a high temperature. A two-step procedure was selected: the gold wool was first heated to 100 °C for 4 minutes to trap Hg vapor as well as to avoid water deposition on gold wool, then heated to a temperature of 500 °C for 20 seconds for releasing Hg⁰ from the amalgam.

Fig. 11.5 shows the Hg absorption signals obtained with 1% *Olea Europaea* suspensions with and without mercury standards added. Due to the enrichment, strong Hg signals with narrow peak shape were observed, giving an increase of sensitivity of more than one order of magnitude. The detection limit (3SD, N=11) was 0.015 µg/g with a blank of 2.5 M HNO₃. The reproducibility of 10 consecutive measurements of 1% *Olea Europaea* suspension was 6%. Reference materials such as *Olea Euroaea*, Cod Muscle and Orchard Leaves were studied. The measured values are in good agreement with the certified values (see Table 11.3).

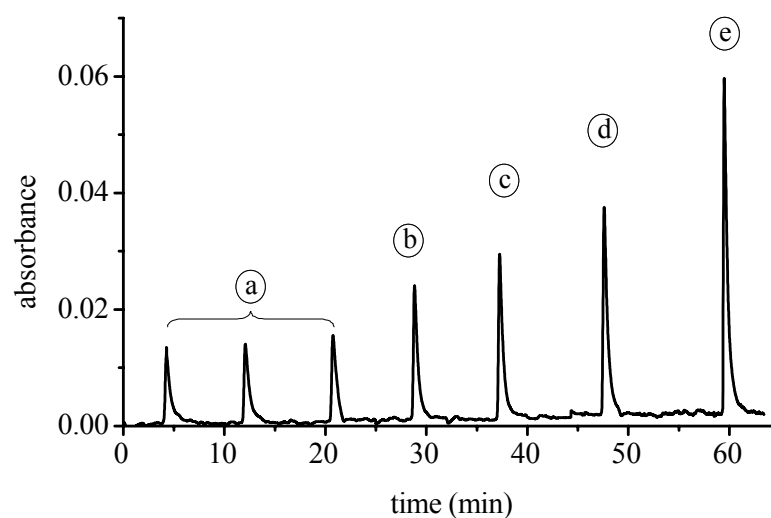


Figure 11.5 Hg signals obtained from analyses of (a) 1% Olea Europaea suspension and (b) to (e) 1% Olea Europaea suspensions with additional standards of 3, 5, 7 and 12 $\mu\text{g/L}$, respectively.

Table 11.3 Certified and experimental concentrations of Hg in reference materials ($\mu\text{g/g}$)

Reference material	Certified value	Measured value
BCR-62, Olea Euroaea	0.28 ± 0.02	0.25 ± 0.02
BCR-422, Cod Muscle	0.559 ± 0.016	0.512 ± 0.023
NBS 1571, Orchard Leaves	0.155 ± 0.015	0.15 ± 0.02

IV. Conclusion

Techniques of direct solid sampling with femtosecond laser ablation and flow acid digestion at high-temperature/high-pressure conditions have been investigated in this thesis. The new techniques are reliable, faster, need less sample material, and allow a more efficient coupling with analytical instruments for on-line analysis.

Differently from nanosecond laser ablation, femtosecond laser ablation produces ultra-fine aerosols which represent the sample composition, can be transported to the analysis instrument (e.g. ICP) without significant losses, and can easily be atomized by an ICP. Since the ablation efficiency is sample dependent, an internal standardization is necessary for a quantitative elemental analysis.

The potential of femtosecond LA-ICP-OES for the non-matrix matched analysis of solid samples has been assessed using three sets of metallic and dielectric standards. The Zn- and Cu-signals and the corresponding Zn/Cu ratios tended to stabilize at laser fluences far above the ablation threshold. Linear calibration curves were obtained within the high fluence range, which implied that fs LA-ICP-OES can suppress fractionation and has the potential for accurate, non-matrix matched analyses.

Spatial distributions Zn and Cu ions in the ICP have been studied using an ICP-MS spectrometer applying femtosecond laser ablation of brass and Al alloys. The ions were not uniformly distributed in the ICP. Large quantities of ions were located in the center of the ICP. The Zn/Cu ratios varied significantly at different spatial positions. Matrix effects on Zn/Cu ratios were small for the metallic samples investigated here. The effects of laser fluences on metallic and dielectric materials were different.

The results obtained with femtosecond laser ablation are promising, in particular, using ICP-OES. However, several investigations have still to be made. Further improvement of the detection sensitivity can be expected if smaller ablation cells which are directly coupled to the ICP-torch are used. By this, the signal dispersion can be reduced and the signal peak can be increased significantly.

The experiment has shown the potential using femtosecond laser ablation for non-matrix matched analyses of Cu and Zn as major and minor matrix constituents. Further experiments have to be made to prove that it is also applicable for other elements than Cu and Zn. Other investigations should also focus on non-matrix matched analyses for elements with low concentrations.

A high-temperature/high-pressure (HTHP) flow digestion system with electrically heated Pt/Ir or Ta capillary was developed. Owing to the mechanical strength of Pt/Ir or Ta material, the system can be applied at extreme conditions (more than 170 bar and up to 340 °C). This temperature is 100 °C higher than that used in microwave-assisted digestion system with a PTFE or PFA reaction coil. Full digestion of biological and environmental materials can be completed within one minute applying these extreme conditions. The capillary could theoretically stand approximately 500,000 digestions without noticeable changes of the capillary properties. The recoveries of most elements were found to be better than 90 % at a digestion temperature of 340 °C. However, the losses of some elements such as Sb, Ag and Ga during digestion limit the applicability for analysis. The glass-free design of the digestion system permits the use of hydrofluoric acid that can improve the dissolution of samples containing silicate. The quasi-close system accomplishes safe and fast sample digestion in a flow mode and exhibits attractive characteristics, such as easy operation, minimal contamination and no loss of volatile elements.

A novel type interface for removing gas interference has been developed to couple the HTHP flow digestion system with elemental detection instruments. This interface contains a porous polypropylene tube and a rod. The rod was set in the tube center to form a 100- μm intermediate layer. This design significantly reduces the gas diffusion distance in the liquid flow and increases the gas escape. When the solution flow passes through this interface, gaseous reaction products, such as CO_2 and NO_x , in the liquid can escape easily through holes of the porous tube. Furthermore, the design decreases the

IV. Conclusion

dead volume of the interface. Therefore, analysis time between 240 and 300 s and a capability of 12-15 samples/h were achieved by coupling with ICP-OES via this interface. The accuracy and reliability of the entire online procedure has been demonstrated by determination of elements in various biological and environmental materials. This interface can also be applied to other flow digestion systems, such as microwave-assisted digestion systems, for effective coupling with ICP-based spectrometers.

Bibliography

- 1 A. Mantaser, *Inductively Coupled Plasma Mass Spectrometry*, 1998, Wiley-VCH, New York.
- 2 H. B. Nicolas, A. Bogaerts and J. A. C. Broekaert, *Anal. Chem.*, 2004, 76, 3313-3336.
- 3 N. H. Bings, A. Bogaerts and J. A. C. Broekaert, *Anal. Chem.*, 2002, 74, 2691-2712.
- 4 J. M. Mermet, *J. Anal. At. Spectrom.*, 2005, 20, 11-16.
- 5 J. H. Macedoen, A. A. Mills and P. B. Farnsworth, *Applied Spectroscopy*, 2004, 58, 463-467.
- 6 G. Knapp and Z. Fresenius, *Anal. Chem.*, 1984, 317, 231-235.
- 7 Z. Fang, S. Xu and G. Tao, *J. Anal. At. Spectrom.*, 1996, 11, 1-24.
- 8 S. J. Hill, T. A. Arowolo, O. T. Butler, J. S. Cresser, C. Harrington and D. L. Miles, *J. Anal. At. Spectrom.*, 2004, 19, 301-330.
- 9 R. T. White, P. Kettish and P. Kainrath, *At. Spectrosc.*, 1998, 19, 187-192.
- 10 F. Vanhaecke, S. Boonen, L. Moens and R. Dams, *J. Anal. At. Spectrom.*, 1997, 12, 125-130.
- 11 J. M. Ren and E. D. Salin, *Spectrochim. Acta, Part B*, 1994, 49, 555-566.
- 12 M. Henyk, N. Vogel, D. Wolframm, A. Tempel and J. Reif, *Appl. Phys. A*, 1999, 69, 355-358.
- 13 M. Gagean and J. M. Mermet, *J. Anal. At. Spectrom.*, 1997, 12, 189-193.
- 14 J. B. Ko, W. Sdorra and K. Niemax, *Fresenius Z. Anal. Chem.*, 1989, 335, 648-651.
- 15 O.V. Borisov, X. L. Mao, A. Fernandez, M. Caetano, R. E. Russo, *Spectrochimica Acta, part B*, 1999, 54, 1351-1365.
- 16 R. E. Russo, X. L. Mao, H. C. Liu, J. Gonzalez and S. S. Mao, *Talanta*, 2002, 57, 425-451.
- 17 V. Margetic, K. Niemax and R. Hergenröder, *Anal. Chem.*, 2003, 75, 3435-3439.
- 18 R. E. Russo, *Appl. Spectrosc.*, 1995, 49, 14A-28A.
- 19 J. D. Winefordner, I. B. Gornushkin, D. Pappas, O. I. Matveev and B. W. Smith, *J. Anal. At. Spectrom.*, 2000, 15, 1161-1189.
- 20 J. Gonzalez, C. Y. Liu, X. L. Mao and R. E. Russo, *J. Anal. At. Spectrom.*, 2004, 19, 1165-1168.
- 21 V. Margetic, A. Pakulev, A. Stockhaus, M. Bolshov, K. Niemax and R. Hergenröder, *Spectrochim. Acta, Part B*, 2000, 55, 1771-1785.
- 22 M. Tibi and K. G. Heumann, *J. Anal. At. Spectrom.*, 2003, 18, 1076-1081.
- 23 J. Koch, A. von Bohlen, R. Hergenröder and K. Niemax, *J. Anal. At. Spectrom.*, 2004, 19, 267-272.

-
- 24 M. Würfels, E. Jackwerth and M. Stoeppler, *Fresenius J. Anal. Chem.*, 1987, 329, 459-461.
- 25 V. Margetic, *Femtosecond Laser Ablation*, dissertation, Dortmund University, 2002.
- 26 B. N. Chichkov, C. Momma, S. Nolte, F. von Alvensleben and A. Tünnermann, *Applied Physics A*, 1996, 63, 109-115.
- 27 D. Bäuerle, *Laser Processing and Chemistry*, 3rd edition, Springer, p209.
- 28 S. S. Mao, F. Quere, S. Guizard, X. Mao, R. E. Russo, G. Petite and P. Martin, *Appl. Phys. A*, 2004, 79, 1695-1709.
- 29 B. Rethfeld, K. Sokolowski-tinten, D. Von Der Linde and S. I. Anisimov, *Applied Physics A*, 2004, 79, 767-769.
- 30 D. Ashkenasi, M. Lorenz, R. Stoian and A. Rosenfeld, *Appl. Surf. Sci.*, 1999, 150, 101-106.
- 31 G. J. Pert, *Physical Review E*, 1995, 51, 4778-4789.
- 32 Holger Dömer, *Hochgeschwindigkeits-Transmissionselektronenmikroskopie zur zeitaufgelösten Untersuchung der Laser ablation dünner Metallfolien*, dissertation, der Technischen Universität Berlin, 2004.
- 33 S. I. Anisimov, B. Kapeliovich and T. Perel'man, *Sovjet Physics JETP*, 1994, 39, 375.
- 34 S. Nolte, C. Momma, H. Jacobs, A. Tünnermann, B. N. Chichkov, B. Wellegehausen and H. Welling, *J. Opt. Soc. Am. B*, 1997, 14, 2716-2722.
- 35 K. Furusawa, K. Takahashi, H. Kumagai, K. Midorikawa and M. Obara, *Applied Physics A*, 1999, 69, 359-366.
- 36 I.v. zhigilei, *Appl. Phys. A*, 2003, 76, 339-350.
- 37 F. Vidal, T. W. Johnston, S. Laville, O. Barthelemy, M. Chaker, B. Le Drogoff, J. Margot and M. Sabsabi, *Physical Review Letters*, 2001, 86, 2573-2576.
- 38 B. R. Graskow, *Design and Development of a Fast Aerosol Size Spectrometer*, dissertation, University of Cambridge, Department of Engineering, 2001.
- 39 W. C. Hinds, *Aerosol Technology*, John Wiley and Sons, New York, USA, 1982.
- 40 P. G. Gormley and M. Kennedy, *Proceedings of the Irish Academy*, 1949, 52A, 163-169.
- 41 I. Y. Chang, W. C. Griffith, L. J. Shyr, H. C. Yeh, R. G. Cuddihy and F. A. Seiler, *Radiation Protection Dosimetry*, 1991, 38, 193-199.
- 42 A. Michels, J. Koch and R. Hergenröder, to be published.
- 43 J. Koch, H. Lindner, A. von Bohlen, R. Hergenröder and K. Niemax, in press.
- 44 A. L. Gray, *Analyst*, 1985, 110, 551-556.
- 45 P. Arrowsmith, *Anal. Chem.*, 1987, 59, 1437-1444.
- 46 D. Günther, S. E. Jackson and H. P. Longerich, *Spectrochimica Acta, Part B*, 1999, 54, 381-409.

-
- 47 R. E. Russo, X. L. Mao, J. J. Gonzalez and S. S. Mao, *J. Anal. At. Spectrom.*, 2002, 17, 1072-1075.
- 48 J. Koch, I. Feldmann, N. Jakubowski and K. Niemax, *Spectrochim. Acta, Part B*, 2002, 57, 975-985.
- 49 C. Liu, X. L. Mao, S. S. Mao, X. Zeng, R. Greif, and R. E. Russo, *Anal. Chem.*, 2004, 76, 379-383.
- 50 S. Ota, M. Vanja and H. Roland, *Anal Bioanal Chem*, 2005, 381, 54-56.
- 51 A. Ciocan, J. Uebbing and K. Niemax, *Spectrochimica Acta*, 1992, 47, 611-617.
- 52 T. Pettke, C. A. Heinrich, A. C. Ciocan and D. Günther, *J. Anal. At. Spectrom.*, 2000, 15, 1149-1155.
- 53 R. E. Russo, X. L. Mao, C. Liu and J. Gonzalez, *J. Anal. At. Spectrom.*, 2004, 19, 1084-1089.
- 54 A. M. Leach and G. M. Hieftje, *Applied Spectroscopy*, 2002, 56, 62-69.
- 55 H. R. Kuhn, M. Guillong and D. Günther, *Anal. Bioanal. Chem.*, 2004, 378, 1069-1074.
- 56 M. Guillong and D. Günther, *J. Anal. At. Spectrom.*, 2002, 17, 831-837.
- 57 H. Lindner, Diploma thesis, University of Dortmund, 2004, to be published.
- 58 J. Koch in preparation.
- 59 J. M. Mermet, *J. Anal. At. Spectrom.*, 2002, 17, 1065-1071.
- 60 B. Hattendorf, C. Latoczy and D. Günther, *Anal. Chem.*, 2003, 75, 341A-347A.
- 61 D. J. Douglas and J. B. French, *J. Anal. At. Spectrom.*, 1988, 3, 743-748.
- 62 A. C. Lazar and P. B. Farnsworth, *Applied Spectroscopy*, 1999, 53, 465-470.
- 63 J. H. Macedone, A. A. Milles and P. B. Farnsworth, *Applied Spectroscopy*, 2004, 58, 463-467.
- 64 D. Günther and B. Hattendorf, *Trends in Anal. Chem.*, 2005, 24, 255-265.
- 65 D. Beauchemin, D. C. Gregoire, D. Günther, V. Karanassios, J. M. Mermet and T. J. Wood, *Discrete sample introduction techniques for inductively coupled plasma mass spectrometry*, 2000, Elsevier.
- 66 E. de Oliveira, *J. Braz. Chem. Soc.*, 2003, 14, 174-182.
- 67 <http://www.shodor.org/UNChem/advanced/kin/arrhenius.html>.
- 68 M. Takenake, S. Kozuka, M. Hayashi, H. Endo, *Analyst*, 1997, 122, 129.
- 69 A. Abu-Samra, J. S. Morris and S. R. Koirtyohann, *Anal. Chem.*, 1975, 47, 1475-1477.
- 70 I. Kojima, T. Uchida and C. Iida, *Anal. Sci.*, 1988, 4, 211.
- 71 E. M. de Moraes Flores, J. S. Barin, J. N. G. Paniz, J. A. Medeiros and G. Knapp, *Anal. Chem.*, 2004, 76, 3525 – 3529.
- 72 P. Schramel, I. Wedler and G. Knapp, *Fresenius J. Anal. Chem.*, 1996, 356, 512-514.
- 73 M. Wasilewska, W. Goessler, M. Zischka, B. Malchin, G. Knapp, *J. Anal. At. Spectrom.*, 2002, 17, 1121-1125.

-
- 74 M. Burguera, J. L. Burguera and O. M. Alarcon, *Anal. Chim. Acta*, 1986, 179, 351–357.
- 75 J. L. Burguera and M. Burguera, *Anal. Chim. Acta*, 1990, 238, 417–421.
- 76 T. J. Gluodenis and J. F. Tyson, *J. Anal. At. Spectrom.*, 1992, 7, 301-306.
- 77 R. E., Sturgeon, S. N. Willie, B. A. Methven, J. W. Lam and H. Matusiewicz, *J. Anal. At. Spectrom.*, 1995, 10, 981-986.
- 78 U. Pichler and A. Haase, G. Knapp, *Anal. Chem.*, 1999, 71, 4050–4055.
- 79 S. K. Luo and H. Berndt, *Spectrochim. Acta, Part B*, 1994, 49, 485-492.
- 80 C. Gräber and H. Berndt, *J. Anal. At. Spectrom.*, 1999, 14, 683-691.
- 81 S. Haiber and H. Berndt, *Fresenius J. Anal. Chem.*, 2000, 368, 52–58.
- 82 P. Jacob and H. Berndt, *J. Anal. At. Spectrom.*, 2002, 17, 1615–1620.
- 83 S. Wu and X. Feng, *Proc. Int. Symp., 9th, Natl. Research Council Canada*, 1997, 257–259.
- 84 S. Recknagel, P. Brätter, A. Tomiak and U. Rösik, *Fresenius J. Anal. Chem.*, 1993, 346, 833–836.
- 85 M. de la Guardia, V. Carbonell, A. Morales-Rubio and A. Salvador, *Talanta*, 1993, 40, 1609-1617.
- 86 S. M. Rahmat Ullah, R. L. Adams, K. Srinivasan and P. K. Dasgupta, *Anal. Chem.*, 2004, 76, 7084-7093.
- 87 Fuhsiang Ko, Shunlong Chen and Mohsiung Yang, *J. Anal. At. Spectrom.*, 1997, 12, 589-595.
- 88 Z. Fang, *Flow Injection Separation and Preconcentration*, VCH Publishers: Weinheim, New York, 1993.
- 89 S. Motomizu, K. Toei, T. Kuwaki, M. Oshima, *Anal. Chem.*, 1987, 59, 2930–2932.
- 90 S. A. Stern, *Polymers for gas separation: the next decade*, *Journal of Membrane Science*, 1994, 94, 1–65.
- 91 E. R. Pereira-Filho, H. Berndt and M. A. Zezzi Arruda, *J. Anal. At. Spectrom.*, 2002, 17, 1308-1315.
- 92 M. Krachler, M. Burow and H. Emons, *the Analyst*, 1999, 124, 777-782.
- 93 M. Krachler and H. Emons, *Fresenius J Anal. Chem.*, 2000, 368, 702-707.
- 94 H. Berndt and J. Yanez, *J. Anal. At. Spectrom.*, 1996, 11, 703-712.
- 95 from <http://www.efm.leeds.ac.uk>
- 96 M. Noack, P. Kölsch, P. Toussaint, P. Druska, J. Caro, *Chemie Ingenieur Technik*, 1998, 70, 992.
- 97 Fred Wiesler, *Ultrapure Water*, May/June, 1996, 27-31.
- 98 M. Yang and E. L. Cussler, “Designing Hollow-Fiber Contactors”, *ALChE Journal*, 1986, 32, 1-5.

Acknowledgements

I am very grateful to my supervisor, Prof. Dr. Kay Niemax, for giving me the opportunity to study in ISAS. I wish to thank him for his support and lots of constructive comments, especially during the writing of my thesis.

I am very appreciative of Dr. Peter Jacob and Dr. Joachim Koch for their guidance, knowledge bestowed upon me, and proofreading my published papers and this thesis.

I wish to thank Prof. Dr. Harald Berndt for sharing his lots of new ideas with me.

It is very pleasant to be a member of the Material Analysis group led by Dr. Roland Hergenröder. I want to thank him for his encouragement.

I have been fortunate enough to work in two research groups. I appreciate the time I have spent with my group members. I thank them for the nice and inspiring working atmosphere. In particular, I would like to thank Mrs. B. Mergler for experimental help, Mr. Helmut Lindner for sharing his knowledge in physics, Dr. Andre Kurowski, Dr. Vanja Hommes and Dr. Manuela Miclea for their great help with the laser system, and Dr. Ota Samek, Mr. Frank Bergers for sharing the fs laser and the lab.

Special thanks also go to Mr. Rolf Brandt for maintaining and running the ICP-MS and Mr. Norman Ahlmann for measuring the crater using the SEM. I would also like to thank Mr. Hans-Marglus Eickmeyer and other colleagues in ISAS for their help.

Sincere thanks go to Prof. Dr. D. Suter for agreeing to be my second supervisor and evaluating this thesis.

I am grateful to Prof. Zhanxia Zhang in Zhongshan (Sun Yat-sen) University for her continuous support.

Finally, I would like to thank my parents for their endless care and my wife Mei Wang for her love, support and accompanying me in Germany.



Curriculum vitae

Name : Qunzhou Bian

Date of Birth: 20 Sept. 1969

Nationality: P. R. China

Marital Status: Married

Education

2002 – 2005: Ph. D, Institute for Analytical Sciences, University of Dortmund, Dortmund, Germany.

1994 – 1997: M.Sc., School of Chemistry and Chemical Engineering, Zhongshan (Sun Yat-sen) University, Guangzhou, China.

Thesis: “The Study of the Analytical Performances and Applications of the Self-constructed CCD-ICP Atomic Emission Spectrograph”.

1987 – 1991: B.Sc., Chemistry Department, Huazhong Normal University, Wuhan, China.

Publications in international journals contributed to this Ph.D thesis

1. Q. Z. Bian, P. Jacob, H. Berndt, K. Niemax, Online Flow Digestion of Biological and Environmental Samples for Inductively Coupled Plasma-Optical Emission Spectroscopy (ICP-OES), *Analytica Chimica Acta*, 2005, 538 (1-2), 323-329.
2. Q. Z. Bian, J. Koch, H. Lindner, R. Hergenröder, and K. Niemax, Non-matrix matched calibration using near infrared femtosecond laser ablation inductively coupled plasma optical emission spectrometry, *J. Anal. At. Spectrom.*, *J. Anal. At. Spectrom.*, 2005, 20, 736-740.
3. Q. Z. Bian, J. Koch, R. Hergenröder, and K. Niemax, preliminary title: Analyses of brass, aluminum and silicate glass using femtosecond laser ablation inductively coupled plasma mass spectrometry, *J. Anal. At. Spectrom.* (to be submitted)